

Virological characteristics of the SARS-CoV-2 XBB variant derived from recombination of two Omicron subvariants

Tomokazu Tamura^{1,30}, Jumpei Ito^{2,30}, Keiya Uriu^{2,3,30}, Jiri Zahradnik^{4,5,30}, Izumi Kida^{6,30}, Hesham Nasser^{7,8,30}, Maya Shofa^{9,10,30}, Yoshitaka Oda^{11,30}, Spyros Lytras^{12,30}, Naganori Nao^{13,14}, Yukari Itakura¹⁵, Sayaka Deguchi¹⁶, Rigel Suzuki¹, Lei Wang^{11,17}, MST Monira Begum⁷, Masumi Tsuda^{11,17}, Yusuke Kosugi^{2,3}, Shigeru Fujita^{2,3}, Kumiko Yoshimatsu¹⁸, Saori Suzuki¹, Hiroyuki Asakura¹⁹, Mami Nagashima¹⁹, Kenji Sadamasu¹⁹, Kazuhisa Yoshimura¹⁹, Yuki Yamamoto²⁰, Tetsuharu Nagamoto²⁰, Gideon Schreiber⁴, The Genotype to Phenotype Japan (G2P-Japan) Consortium, Terumasa Ikeda⁷, Takasuke Fukuhara^{1,21,22}, Akatsuki Saito^{9,10,23}, Shinya Tanaka^{11,17*}, Keita Matsuno^{6,14,24*}, Kazuo Takayama^{16,21*}, Kei Sato^{2,3,25,26,27,28,29*}

¹Department of Microbiology and Immunology, Faculty of Medicine, Hokkaido University, Sapporo, Japan

²Division of Systems Virology, Department of Microbiology and Immunology, The Institute of Medical Science, The University of Tokyo, Tokyo, Japan

³Graduate School of Medicine, The University of Tokyo, Tokyo, Japan

⁴Department of Biomolecular Sciences, Weizmann Institute of Science, Rehovot, Israel

⁵First Medical Faculty at Biocev, Charles University, Vestec-Prague, Czechia

⁶Division of Risk Analysis and Management, International Institute for Zoonosis Control, Hokkaido University, Sapporo, Japan

⁷Division of Molecular Virology and Genetics, Joint Research Center for Human Retrovirus infection, Kumamoto University, Kumamoto, Japan

⁸Department of Clinical Pathology, Faculty of Medicine, Suez Canal University, Ismailia, Egypt

⁹Department of Veterinary Science, Faculty of Agriculture, University of Miyazaki, Miyazaki, Japan

¹⁰Graduate School of Medicine and Veterinary Medicine, University of Miyazaki, Miyazaki, Japan

¹¹Department of Cancer Pathology, Faculty of Medicine, Hokkaido University, Sapporo, Japan

¹²Medical Research Council-University of Glasgow Centre for Virus Research, Glasgow, UK

¹³Division of International Research Promotion, International Institute for Zoonosis Control, Hokkaido University, Sapporo, Japan

¹⁴One Health Research Center, Hokkaido University, Sapporo, Japan

¹⁵Division of Molecular Pathobiology, International Institute for Zoonosis Control, Hokkaido University, Sapporo, Japan

¹⁶Center for iPS Cell Research and Application (CiRA), Kyoto University, Kyoto, Japan

44 ¹⁷Institute for Chemical Reaction Design and Discovery (WPI-ICReDD),
 45 Hokkaido University, Sapporo, Japan
 46 ¹⁸Institute for Genetic Medicine, Hokkaido University, Sapporo, Japan
 47 ¹⁹Tokyo Metropolitan Institute of Public Health, Tokyo, Japan
 48 ²⁰HiLung, Inc., Kyoto, Japan
 49 ²¹AMED-CREST, Japan Agency for Medical Research and Development
 50 (AMED), Tokyo, Japan
 51 ²²Laboratory of Virus Control, Research Institute for Microbial Diseases, Osaka
 52 University, Suita, Japan
 53 ²³Center for Animal Disease Control, University of Miyazaki, Miyazaki, Japan
 54 ²⁴International Collaboration Unit, International Institute for Zoonosis Control,
 55 Hokkaido University, Sapporo, Japan
 56 ²⁵International Research Center for Infectious Diseases, The Institute of Medical
 57 Science, The University of Tokyo, Tokyo, Japan
 58 ²⁶International Vaccine Design Center, The Institute of Medical Science, The
 59 University of Tokyo, Tokyo, Japan
 60 ²⁷Graduate School of Frontier Sciences, The University of Tokyo, Kashiwa,
 61 Japan
 62 ²⁸Collaboration Unit for Infection, Joint Research Center for Human Retrovirus
 63 infection, Kumamoto University, Kumamoto, Japan
 64 ²⁹CREST, Japan Science and Technology Agency, Kawaguchi, Japan
 65 ³⁰These authors contributed equally
 66
 67 *Corresponding authors:
 68 tanaka@med.hokudai.ac.jp (Shinya Tanaka),
 69 matsuk@czc.hokudai.ac.jp (Keita Matsuno),
 70 kazuo.takayama@cira.kyoto-u.ac.jp (Kazuo Takayama),
 71 KeiSato@g.ecc.u-tokyo.ac.jp (Kei Sato)
 72
 73 **Conflict of interest:** Yuki Yamamoto and Tetsuharu Nagamoto are founders
 74 and shareholders of HiLung, Inc. Yuki Yamamoto is a co-inventor of patents
 75 (PCT/JP2016/057254; "Method for inducing differentiation of alveolar epithelial
 76 cells", PCT/JP2016/059786, "Method of producing airway epithelial cells"). The
 77 other authors declare that no competing interests exist.
 78
 79 **Short title:** Characteristics of SARS-CoV-2 XBB (33/50 characters)
 80 **Keywords:** SARS-CoV-2; COVID-19; Omicron; XBB; recombination;
 81 transmissibility; immune resistance; pathogenicity

82 **Abstract** (139/150 words)

83 In late 2022, the SARS-CoV-2 Omicron subvariants have highly diversified, and
 84 XBB is spreading rapidly around the world. Our phylogenetic analyses
 85 suggested that XBB emerged by recombination of two co-circulating BA.2
 86 lineages, BJ.1 and BM.1.1.1 (a progeny of BA.2.75), during the summer of 2022
 87 around India. *In vitro* experiments revealed that XBB is the most profoundly
 88 resistant variant to BA.2/5 breakthrough infection sera ever and is more
 89 fusogenic than BA.2.75. Notably, the recombination breakpoint is located in the
 90 receptor-binding domain of spike, and each region of recombined spike
 91 conferred immune evasion and augmented fusogenicity to the XBB spike. Finally,
 92 the intrinsic pathogenicity of XBB in hamsters is comparable to or even lower
 93 than that of BA.2.75. Our multiscale investigation provided evidence suggesting
 94 that XBB is the first documented SARS-CoV-2 variant increasing its fitness
 95 through recombination rather than single mutations.

96 Introduction

97 The SARS-CoV-2 Omicron variant is the current variant of concern since the end
 98 of 2021 (ref.¹). As of December 2022, recently emerging Omicron subvariants
 99 are under convergent evolution: recently emerging variants acquired
 100 substitutions at the same residues of the spike (S) protein, such as R346, K444,
 101 L452, N460, and F486^{2,3}. For instance, Omicron BQ.1.1 variant, which is a
 102 descendant of Omicron BA.5 and is currently becoming predominant in the
 103 Western countries¹, possesses all convergent substitutions, such as R346T,
 104 K444T, L452R, N460K, and F486V. Recent studies including ours suggested
 105 that L452R⁴⁻⁹, N460K^{2,6,10,11}, and R346T² increase the binding affinity of
 106 SARS-CoV-2 S protein to human angiotensin-converting enzyme 2 (ACE2), the
 107 receptor for viral infection, while R346T^{12,13}, K444T¹² and F486V^{2,4,5,12,14,15}
 108 contribute to evade antiviral humoral immunity induced by vaccination and
 109 natural SARS-CoV-2 infection. Similar to the observations in BA.5 (ref.⁵) and
 110 BA.2.75 (ref.¹⁰), combinational substitutions in S protein (1) to evade antiviral
 111 humoral immunity in exchange for the decrease of ACE2 binding affinity (e.g.,
 112 F486V) and (2) to enhance ACE2 binding affinity to compensate the decreased
 113 affinity by immune evasion substitution (e.g., L452R and N460K) has been
 114 frequently observed in recently emerging Omicron subvariants including BQ.1.1.
 115 These observations suggest that acquiring these two types of substitutions in the
 116 S protein is a trend for recently emerging Omicron subvariants to spread more
 117 efficiently than prior ones.

118 In addition to the diversification and subsequent convergent evolution
 119 of emerging Omicron subvariants (e.g., BQ.1.1), a recombinant variant, called
 120 XBB, has recently emerged. The Omicron XBB variant likely originated by the
 121 recombination of two BA.2 descendants, BJ.1 and BM.1.1.1 (a progeny of
 122 BA.2.75)¹⁶. While the BQ.1 lineage is becoming predominant in Europe, XBB
 123 has become predominant in India and Singapore and is spreading several
 124 countries¹⁷. As of October 28, 2022, the WHO classifies XBB as an Omicron
 125 subvariant under monitoring¹. Recent studies including ours have revealed the
 126 virological features of BQ.1 (refs.^{2,13,18}). However, the features of XBB, another
 127 Omicron subvariants of concern, are not fully elucidated. In this study, we
 128 elucidated the virological characteristics of XBB, particularly its transmissibility,
 129 immune resistance, ACE2 binding affinity, infectivity, fusogenicity and intrinsic
 130 pathogenicity in a hamster model.

Results

Evolution and epidemics of the XBB variant

As of December 2022, most of the prevalent Omicron lineages, including BA.5, are descendants of BA.2 (**Fig. 1a**). Of these, highly diversified BA.2 subvariants, such as BA.2.75 and BJ.1, have emerged in South Asia and are referred to as the second-generation BA.2 variants (**Fig. 1a**). Recently, the XBB variant emerged as a recombinant lineage between the second generation BA.2 variants, BJ.1 and BM.1.1.1 (BA.2.75.3.1.1.1; a descendant of BA.2.75)¹⁶ (**Fig. 1a**). XBB harbors the S substitutions R346T, N460K, and F486S, which have been convergently acquired during the Omicron evolution (**Fig. 1b**)². To trace the recombination event that led to the emergence of the XBB variant, we retrieved all SARS-CoV-2 sequences deposited to GISAID (as of October 3, 2022) with PANGO lineage designation matching BJ.1, BM.1, XBB, and all their descendant lineages (including BM.1.1, BM.1.1.1, and XBB.1). Recombination analysis on the aligned set of sequences, using RDP5 (ref.¹⁹), robustly picks up a single recombination breakpoint unique to all XBB sequences at the genomic position 22,920 (matching the Wuhan-Hu-1 reference genome) (**Fig. 1c**). No evidence of recombination was found in the BJ.1 and BM.1 sequences in the dataset. Consistent with the result of the RDP5 analysis, the visual inspection of the nucleotide differences between the consensus sequences of XBB, BJ.1, and BM.1 (including BM.1.1 and BM.1.1.1) clearly illustrates that the XBB identity to BJ.1 ends at the genome position 22,942 and the XBB identity to BM.1 starts after position 22,896 (**Fig. 1c**). Together, our recombination analysis suggests that the recombination breakpoint is between positions 22,897 and 22,941, within the receptor binding domain (RBD) of S protein (corresponding to amino acid positions 445-460) (**Fig. 1c**).

We then split the sequence alignment at position 22,920 to determine the evolutionary history of each non-recombinant segment of the XBB genomes. The phylogenetic reconstructions recapitulate the recombination results, with the 5' end major parental sequence being derived from the BJ.1 clade and the 3' end minor parental sequence from the BM.1.1.1 clade (**Fig. 1d**). Using the longer 5' end non-recombinant part of these genomes, we estimated the emergence date of XBB based on the inferred root-to-tip regression (see **Methods**) (**Fig. 1d**). This analysis suggests that the XBB clade stemmed from the major BJ.1 clade in the span from July 22 to August 5, 2022 (**Fig. 1d**). Furthermore, we inferred the emergence region of XBB by a discrete ancestral state reconstruction utilizing a Markov model (see **Methods**). Most of the earlier isolates of XBB were sampled in India, and our analysis suggests that the ancestral state (i.e., the circulating region) of the most recent common ancestor (MRCA) of XBB sequences is likely India (**Fig. 1e and Extended Data Fig. S1b**). Together, our analyses suggest

171 that XBB emerged through the recombination of two co-circulating lineages,
172 BJ.1 and BM.1.1.1, during the summer of 2022 in India or neighboring countries.

173 To trace the shift of viral fitness during the evolution of Omicron leading
174 to the emergence of XBB, we estimated the effective reproduction number (R_e)
175 of XBB-related variants based on the epidemic data of SARS-CoV-2 in India
176 (from June 1 to November 15, 2022) (**Fig. 1f and Extended Data Fig. S1c and**
177 **Supplementary Table 1**). BJ.1 and BM.1/BM.1.1/BA.1.1.1 showed higher R_e
178 compared with their parental lineages, BA.2.10 and BA.2.75, respectively.
179 Furthermore, the R_e value of XBB is 1.23- and 1.20-times higher than those of
180 the parental BJ.1 and BM.1.1.1, respectively (**Fig. 1f and Extended Data Fig.**
181 **S1c and Supplementary Table 1**). Importantly, this is the first documented
182 example of a SARS-CoV-2 variant increasing its fitness through recombination
183 rather than single mutations.

184 As of December 2022, two viral lineages are expanding their epidemics
185 around the world: BQ.1 lineages and XBB lineages. To investigate the
186 prevalence of these two lineages in various geographic regions, we estimated
187 the epidemic frequency of each variant as of November 15, 2022, in each county
188 (**Fig. 1g and Supplementary Table 2**). BQ.1 lineages have spread and reached
189 dominance in European, American, and African countries, probably reflecting
190 the likelihood that BQ.1 emerged from the African continent²⁰ (**Fig. 1g**). On the
191 other hand, XBB lineages have spread and reached dominance in South and
192 Southeast Asian countries, such as India, Singapore, and Indonesia, reflecting
193 the fact that XBB originated around India (**Fig. 1e,g**). Furthermore, we
194 constructed a hierarchical Bayesian model and estimated the global average
195 and country-specific R_e values of XBB lineages according to the epidemic data
196 of countries where XBB lineages cocirculated with BQ.1 lineages (**Fig. 1h,i,**
197 **Extended Data Fig. S1d and Supplementary Table 3**). Our analysis shows
198 that the R_e values of XBB and XBB.1 (i.e., XBB harboring S:G252V) are 1.24
199 and 1.26-times higher than that of BA.5 and are comparable with those of BQ.1
200 and BQ.1.1 (**Fig. 1h and Extended Data Fig. S1d**). Together, our analyses
201 show that both BQ.1 and XBB lineages, exhibiting a similar advantage in viral
202 fitness, are becoming predominant in the Western and Eastern Hemispheres,
203 respectively.

204

205 Immune resistance of XBB

206 To investigate the virological features of XBB, we first evaluated the immune
207 resistance of XBB using HIV-1-based pseudoviruses. In the present study, we
208 used the major S haplotype of XBB lineages as of October 3, 2022,
209 corresponding to the S protein of XBB.1, for the following experiments (hereafter
210 we simply refer to XBB.1 as XBB). In the case of breakthrough BA.2 infection
211 sera, BA.2.75 did not exhibit significant resistance when compared to BA.2 (**Fig.**

212 **2a**), which is consistent with our prior study¹⁰. In contrast, we found that XBB
213 exhibits a profound (30-fold) resistance to breakthrough BA.2 infection sera
214 ($P=0.0002$, **Fig. 2a**). To determine amino acid substitutions conferring the
215 profound resistance to the breakthrough anti sera, we constructed the BA.2 S
216 mutants which harbor respective single substitutions present in XBB. We did not
217 analyze the substitutions present also in BA.2.75 (e.g., G446S) since we have
218 already analyzed these substitutions in our previous study¹⁰. As shown in **Fig.**
219 **2a**, several substitutions such as V83A (2.1-fold, $P=0.0034$), Y144del (2.9-fold,
220 $P=0.0002$), Q183E (2.0-fold, $P=0.0039$), R346T (2.1-fold, $P=0.0005$), L368I
221 (1.8-fold, $P=0.042$), V445P (2.1-fold, $P=0.0002$), F486S (3.0-fold, $P=0.0002$),
222 and F490S (2.7-fold, $P=0.024$) conferred significant resistance to breakthrough
223 BA.2 infection sera. Because the immune resistance conferred by respective
224 substitution is relatively minor when compared to the resistance of XBB (**Fig. 2a**),
225 our data suggest that multiple substitutions in the XBB S cooperatively
226 contribute to the resistance against humoral immunity induced by breakthrough
227 BA.2 infection.

228 Consistent with our previous study¹⁰, BA.2.75 showed a statistically
229 significant (1.8-fold) resistance to breakthrough BA.5 infection sera when
230 compared to BA.2 ($P=0.0016$, **Fig. 2b**). Moreover, XBB exhibited a profound
231 (13-fold) resistance to breakthrough BA.5 infection sera ($P<0.0001$, **Fig. 2b**).
232 Neutralization assay using the pseudoviruses with BA.2 derivatives revealed
233 that the Y144del mutation (1.8-fold, $P=0.016$) resulted in the resistance to
234 breakthrough BA.5 infection sera (**Fig. 2b**). Furthermore, in our previous study,
235 we showed that G446S, which is a common substitution of BA.2.75 and XBB,
236 conferred immune resistance to breakthrough BA.5 infection sera¹⁰. Together,
237 these observations suggest that these two mutations (Y144del and G446S)
238 cooperatively contribute to the resistance against humoral immunity induced by
239 breakthrough BA.5 infection.

240 To further evaluate the antigenicity of XBB S, we used the sera
241 obtained from infected hamsters at 16 days post infection (d.p.i.). As shown in
242 **Fig. 2c**, XBB exhibited profound resistance to the sera obtained from hamsters
243 infected with BA.2, BA.5, BQ.1.1, and BA.2.75. Moreover, XBB infection hamster
244 sera exhibited remarkable antiviral effect against only XBB (**Fig. 2c**). The
245 cartography based on the neutralization dataset using hamster sera (**Fig. 2c**)
246 showed that the cross-reactivity of each Omicron subvariant is correlated to their
247 phylogenetic relationship (**Fig. 1a**). and the antigenicity of XBB is distinct from
248 the other Omicron subvariants tested (**Fig. 2d**). These observations suggest that
249 XBB is antigenically different from the other Omicron subvariants including
250 BQ.1.1, and therefore, remarkably evades the BA.2/5 infection-induced herd
251 immunity in the human population.

252

253 **ACE2 binding affinity of XBB S**

254 We then evaluated the features of XBB S that potentially affect viral infection and
 255 replication. Yeast surface display assay^{2,10,21,22} showed that the binding affinity
 256 of XBB S RBD to human ACE2 receptor (1.00 ± 0.069) is significantly lower than
 257 that of ancestral BA.2 S RBD (1.49 ± 0.054) (**Fig. 3a**). As described above (**Fig.**
 258 **1a–c**), the four RBD substitutions in XBB compared to BA.2, D339H, G446S,
 259 N460K and R493Q, are common to BA.2.75 since a part of RBD of XBB S is
 260 derived from the BA.2.75/BM.1 lineage. In our previous studies^{2,10}, we
 261 demonstrated that the N460K substitution augments ACE2 binding affinity. To
 262 address whether other substitutions in the XBB S affect the binding affinity of S
 263 RBD to human ACE2, we prepared a repertoire of BA.2 S RBD that possesses
 264 an XBB-specific substitution compared to BA.2. Consistent with our recent
 265 study^{2,10}, the R346T substitution, which is common in both XBB and BQ.1.1,
 266 significantly increased the binding affinity of BA.2 S RBD to human ACE2 (**Fig.**
 267 **3a**). Additionally, the L368I substitution also augmented ACE2 binding affinity
 268 (**Fig. 3a**). On the other hand, the F486S substitution significantly decreased
 269 ACE2 binding affinity (**Fig. 3a**). Because the F486V substitution also decreased
 270 ACE2 binding affinity⁵, our data suggest that the amino acid substitution at F486
 271 leads to attenuated ACE2 binding affinity. Our results suggested that the
 272 enhanced binding affinity of XBB S RBD compared to BA.2 S RBD is attributed
 273 to at least three substitutions in the RBD: R346T, L368I and N460K^{2,10}.
 274 Nevertheless, the K_D value of XBB S RBD was clearly higher than that of
 275 BA.2.75 S RBD (0.18 ± 0.069) (**Fig. 3a**). In our prior study¹⁰, we showed that the
 276 D339H substitution contributes to the augment of ACE2 binding affinity only
 277 when the backbone is the BA.2.75 S RBD. Therefore, the profound binding
 278 affinity of BA.2.75 S RBD to human ACE2 would be attributed to the
 279 conformation that is composed of multiple substitutions in the BA.2.75 S RBD.

280 We next assessed viral infectivity using pseudoviruses. As shown in
 281 **Fig. 3b**, the infectivity of XBB pseudovirus was 7.6-fold greater than that of BA.2
 282 pseudovirus. Consistent with the results of yeast surface display assay (**Fig. 3a**),
 283 two substitutions in the RBD, R346T (1.9-fold) and L368I (2.2-fold), significantly
 284 increased pseudovirus infectivity (**Fig. 3b**). Additionally, although two
 285 substitutions in the NTD, Y144del (0.18-fold) and G252V (0.54-fold), significantly
 286 decreased pseudovirus infectivity, a substitution in the NTD, V83A (3.3-fold),
 287 significantly increased (**Fig. 3b**). Altogether, our results suggest that the XBB S
 288 augments its infectious potential through the multiple substitutions in the RBD
 289 (R346T, L368I and N460K) and NTD (V83A).

290 To assess the association of TMPRSS2 usage with the increased
 291 pseudovirus infectivity of XBB, we used HEK293-ACE2/TMPRSS2 cells and
 292 HEK293-ACE2 cells, on which endogenous surface TMPRSS2 is undetectable²³,
 293 as target cells. As shown in **Fig. 3c**, the infectivity of XBB pseudovirus was not

increased by TMPRSS2 expression, suggesting that TMPRSS2 is not associated with an increase in the infectivity of XBB pseudovirus.

Fusogenicity of XBB S

The fusogenicity of XBB S was measured by the SARS-CoV-2 S-based fusion assay^{2,5,10,23-28}. We first assessed the fusogenicity of BA.2.75. Consistent with previous studies^{10,18}, the BA.2.75 S exhibited higher fusogenicity than the BA.2 S (**Extended Data Fig. 2a,b**). The assay using the BA.2 S derivatives that harbor respective BA.2.75-specific substitutions revealed that only the N460K substitution significantly increased fusogenicity (**Extended Data Fig. 2b**). We then assessed the fusogenicity of XBB S. As shown in **Fig. 3d**, the surface expression level of XBB was significantly lower than those of BA.2 and BA.2.75. The S-based fusion assay showed that the XBB S is significantly more fusogenic than BA.2 S (2.2-fold) and BA.2.75 S (1.5-fold) (**Fig. 3e**). To assess the determinant substitutions in the XBB S that are responsible for augmented fusogenicity, we used the BA.2 S-based derivatives that harbor respective XBB-specific substitutions. We revealed that particularly two substitutions, V83A and R346T, significantly increased fusogenicity (**Fig. 3e**). Together with the experiments focusing on BA.2.75 S (**Extended Data Fig. 2b**), our results suggest that two substitutions in the RBD (R346T and N460K) and a substitution in the NTD (V83A) contribute to the augmented fusogenicity of XBB S.

Virological characteristics of XBB *in vitro*

To investigate the growth kinetics of XBB in *in vitro* cell culture systems, we inoculated clinical isolates of BA.2²³, BA.2.75¹⁰, and XBB into multiple cell cultures. The growth kinetics of XBB in Vero cells (**Fig. 3f**), Calu-3 cells (**Fig. 3h**), human airway organoid-derived air-liquid interface (AO-ALI) system (**Fig. 3i**), and human induced pluripotent stem cell (iPSC)-derived airway epithelial cells (**Fig. 3j**) were comparable with those of BA.2.75. On the other hand, XBB more efficiently expanded in VeroE6/TMPRSS2 cells than BA.2.75 (**Fig. 3g**). Similar to our previous study¹⁰, the growth of BA.2.75 was significantly greater than that of BA.2 in human iPSC-derived alveolar epithelial cells (**Fig. 3k**). However, XBB was less replicative than BA.2.75 in this culture system (**Fig. 3k**).

To quantitatively assess the impact of XBB infection on the airway epithelial-endothelial barriers, we used an airway-on-a-chips system^{2,10,29,30}. By measuring the amount of virus that invades from the top channel (**Fig. 3l, left**) to the bottom channel (**Fig. 3l, right**), we are able to evaluate the ability of viruses to disrupt the airway epithelial-endothelial barriers. Notably, the percentage of virus that invaded the bottom channel of XBB-infected airway-on-chips was significantly higher than that of BA.2.75-infected airway-on-chips (**Fig. 3m**).

334 Together with the findings of S-based fusion assay (**Fig. 3e**), these results
335 suggest that XBB is higher fusogenic than BA.2.75.

336

337 **Virological characteristics of XBB *in vivo***

338 To investigate the virological features of XBB *in vivo*, we inoculated clinical
339 isolates of Delta²⁶, BA.2.75¹⁰, and XBB. Consistent with our previous
340 studies^{2,10,25,26}, Delta infection resulted in weight loss (**Fig. 4a, left**). On the other
341 hand, the body weights of BA.2.75- and XBB-infected hamsters were stable and
342 comparable (**Fig. 4a, left**). We then analyzed the pulmonary function of infected
343 hamsters as reflected by two parameters, enhanced pause (Penh) and the ratio
344 of time to peak expiratory flow relative to the total expiratory time (Rpef). Among
345 the four groups, Delta infection resulted in significant differences in these two
346 respiratory parameters compared to XBB (**Fig. 4a, middle and right**),
347 suggesting that XBB is less pathogenic than Delta. In contrast, although the
348 Penh and Rpef values of XBB-infected hamsters were significantly different from
349 those of uninfected hamsters, these were comparable to those of
350 BA.2.75-infected hamsters (**Fig. 4a, middle and right**). These observations
351 suggest that the pathogenicity of XBB is comparable to that of BA.2.75.

352 To address the viral spread in hamsters, we measured the viral RNA
353 load in the oral swab. Although the viral RNA loads of the hamsters infected with
354 XBB were significantly lower than those infected with Delta, there was no
355 statistical difference between XBB and BA.2.75 (**Fig. 4b, left**). To assess the
356 efficacy of viral spread in the respiratory tissues, we collected the lungs of
357 infected hamsters at 2 and 5 d.p.i. and separated them into the hilum and
358 periphery regions. However, the viral RNA loads in both lung hilum and
359 periphery of XBB-infected hamsters were significantly lower than those of
360 BA.2.75- and Delta-infected hamsters (**Fig. 4b, middle and right**), suggesting
361 that XBB less efficiently spreads in the lungs of infected hamsters than BA.2.75
362 and XBB. We then investigated the viral spread in the respiratory tissues by
363 immunohistochemical (IHC) analysis targeting viral nucleocapsid (N) protein. As
364 shown in **Fig. 4c and Extended Data Fig. 3a**, the percentage of N-positive cells
365 in the lungs of XBB-infected hamsters was significantly lower than those of
366 BA.2.75- and Delta-infected hamsters. These data suggest that the spreading
367 efficiency of XBB in the lungs of infected hamsters is comparable with or even
368 lower than that of BA.2.75.

369

370 **Intrinsic pathogenicity of XBB**

371 To investigate the pathogenicity of XBB in the lung, the formalin-fixed right lungs
372 of infected hamsters were analyzed by carefully identifying the four lobules and
373 main bronchus and lobar bronchi sectioning each lobe along with the bronchial
374 branches. Histopathological scoring was performed as described in the previous

375 studies^{2,5,10,23,25,26}. Briefly, bronchitis or bronchiolitis, hemorrhage or congestion,
 376 alveolar damage with epithelial apoptosis and macrophage infiltration, type II
 377 pneumocytes and the area of the hyperplasia of large type II pneumocytes were
 378 evaluated by certified pathologists and the degree of these pathological findings
 379 were arbitrarily scored using a four-tiered system as 0 (negative), 1 (weak), 2
 380 (moderate), and 3 (severe)^{2,5,10,23,25,26}. Similar to our previous studies^{2,10,25,26},
 381 four out of the five histological parameters as well as the total score of
 382 Delta-infected hamsters were significantly greater than those of XBB-infected
 383 hamsters (**Fig. 4e**). When we compared the histopathological scores of two
 384 Omicron subvariants, the scores of type II pneumocytes and the area of the
 385 hyperplasia of large type II pneumocytes, and total histology score of
 386 XBB-infected hamsters were comparable with those of BA.2.75-infected
 387 hamsters (**Fig. 4e**). Altogether, these histopathological analyses suggest that
 388 the intrinsic pathogenicity of XBB is lower than that of Delta and comparable with
 389 that of BA.2.75.

390 Discussion

391 Here, we illuminated the evolutionary and epidemic dynamics of XBB variant, a
 392 recombinant lineage rapidly spreading around the world. Our phylogenetic
 393 analyses suggested that XBB emerged through the recombination of two
 394 co-circulating BA.2 lineages, BJ.1 and BM.1.1.1 (a progeny of BA.2.75), during
 395 the summer of 2022 in India or its neighboring countries (**Fig. 1**). Furthermore,
 396 XBB shows substantially higher R_e than the parental lineages, suggesting that
 397 the recombination event increased R_e (i.e., viral fitness). To our knowledge, this
 398 is the first documented example of a SARS-CoV-2 variant increasing its fitness
 399 through recombination rather than single mutations. Furthermore, we showed
 400 that the R_e values of XBB lineages are comparable with or slightly higher than
 401 those of BQ.1 lineages, and XBB and BQ.1 lineages are becoming dominants in
 402 Eastern and Western Hemisphere, respectively. Since XBB lineages are rapidly
 403 spreading also in Western countries such as the USA, this regional difference is
 404 likely explained simply by the distance from the emergence regions of these
 405 lineages rather than caused by the fact that viral fitness changes depending on
 406 circulated regions. Together, although XBB now circulates mainly in countries
 407 around India, this variant has a potential to spread worldwide in the near future.

408 Compared to BA.5, BA.2.75 and even BQ.1.1 (ref.²), the most
 409 remarkable feature of XBB is the profound resistance to antiviral humoral
 410 immunity induced by breakthrough infections of prior Omicron subvariants (**Fig.**
 411 **2**). In fact, our analyses showed that 10 out of 14 breakthrough BA.2 infection
 412 sera and 9 out of 20 breakthrough BA.5 infection sera fail to neutralize XBB. The
 413 neutralization experiments using single mutants showed that multiple
 414 substitutions in the XBB S protein cooperatively contribute to the immune
 415 resistance of XBB, and particularly, not only the substitutions in the RBD but also
 416 at least a mutation in the NTD, Y144del, closely associates with the immune
 417 resistant property of XBB. The effect of Y144del mutation on immune resistance
 418 is reported in a recent study by Cao et al.¹², and this mutation has been
 419 observed in previous variants of concern such as Alpha and Omicron BA.1.
 420 Furthermore, we previously showed that the Mu variant, one of the previous
 421 variants of interest, also has a mutation in the region including Y144 (i.e.,
 422 YY144-145TSN), which contributes to the robust immune escape of this
 423 variant^{31,32}. Additionally, the region including Y144 is proposed that it is one of
 424 the major epitopes of NTD targeting neutralization antibodies³³. Together, these
 425 observations suggest that Y144del mutation in XBB S contributed to escape
 426 from these NTD targeting neutralization antibodies.

427 A series of our previous studies^{2,5,10} showed that the substitutions in S
 428 proteins associating with the escape from humoral immunity tend to lead to
 429 acquire substitutions enhancing the ACE2 binding affinity or viral infectivity
 430 probably to compensate for the negative effects of the immune

431 escape-associated substitutions on the ACE2 binding affinity. In the present
432 study, we show that XBB harbors both the immune escape-associated
433 substitutions (i.e., Y144del and F486S) and the infectivity-enhancing
434 substitutions (i.e., V83A and N460K). Importantly, XBB emerged through
435 recombination in the S gene, and Y144del and V83A are located on the 5'
436 recombinant fragment while F486S and N460K are on the 3' fragment. This
437 means that XBB acquired two sets of a pair of immune escape-associated and
438 infectivity-enhancing substitutions by only one recombination event. Harboring
439 the two sets of the substitution pairs would be one of the causes why XBB shows
440 higher R_e than other Omicron subvariants. Together, although XBB emerged via
441 a unique evolutionary pathway, our data suggest that XBB also follows the same
442 evolutionary rule with other Omicron subvariants.

443 Although BQ.1.1, another Omicron subvariant of concern at the end of
444 2022, acquired these two types of mutation by convergent substitutions², XBB
445 acquired them by a recombination event. In terms of the evolutionary strategy to
446 acquire these two types of mutations, XBB emerged in a unique way.

447 In our previous studies focusing on some Omicron subvariants such as
448 BA.1 (ref.²⁵), BA.2 (ref.²³), BA.5 (ref.⁵), and BA.2.75 (ref.¹⁰), viral fusogenicity in
449 *in vitro* experimental setup was well correlated to viral intrinsic pathogenicity in a
450 hamster model. However, although the fusogenicity of XBB was greater than
451 that of BA.2.75, one of the parental lineages of XBB, the intrinsic pathogenicity
452 of XBB was comparable or even lower than that of BA.2.75. The discrepancy
453 between viral fusogenicity and intrinsic pathogenicity was also observed in
454 another Omicron subvariant of concern at the end of 2022, BQ.1.1 (ref.²). The
455 discrepancy between viral fusogenicity and intrinsic pathogenicity may be
456 explained by at least three possibilities. First, certain mutations in the non-S
457 region of the XBB genome can attenuate viral pathogenicity augmented by the
458 higher fusogenicity compared with BA.2.75. There are at least seven
459 substitutions in the non-S region of XBB when compared to that of BA.2.75, and
460 some of these mutations may attenuate the viral intrinsic pathogenicity
461 (**Extended Data Fig. 1a**). Second, a theoretical study by Sasaki, Lion, and
462 Boots provided a possibility that antigenic escape can augment viral
463 pathogenicity³⁴. Since we demonstrated that at least two descendants of BA.2,
464 BA.5 (ref.⁵) and BA.2.75 (ref.¹⁰), increased their intrinsic pathogenicity, this
465 theory may explain the evolution of Omicron. More importantly, this theory also
466 predicts that there is a limitation to increase viral pathogenicity³⁴. Together with
467 our observations, it might be possible to assume that the pathogenicity of
468 Omicron lineage already reaches a plateau. Third, in the cases of BQ.1.1 (ref.²)
469 and XBB, it might be possible that the tropism and affinity of S proteins of these
470 variants are different between human ACE2 and hamster ACE2, and therefore,
471 a hamster model may not reproduce the human condition.

472 In summary, our results suggested that XBB is highly transmissible and
 473 resistant to the antiviral humoral immunity induced by breakthrough infections of
 474 prior Omicron variants. Although various “local variants” including XBB have
 475 simultaneously and convergently emerged in late 2022, local variants showing a
 476 higher transmissibility will eventually spread to the whole world, like XBB. Therefore,
 477 continued in-depth viral genomic surveillance and real-time evaluation of the risk
 478 of newly emerging SARS-CoV-2 variants, even though considered local variants
 479 at the time of emergence, should be crucial.

480 **Author Contributions**

481 Jumpei Ito performed bioinformatics, modeling, and statistical analysis.
 482 Jumpei Ito and Spyros Lytras performed phylogenetic analyses.
 483 Keiya Uriu, Hesham Nasser, Maya Shofa, Sayaka Deguchi, MST Monira Begum,
 484 Yusuke Kosugi, Shigeru Fujita, Terumasa Ikeda, Akatsuki Saito and Kazuo
 485 Takayama performed cell culture experiments.
 486 Tomokazu Tamura, Izumi Kida, Naganori Nao, Yukari Itakura, Rigel Suzuki,
 487 Kumiko Yoshimatsu, Saori Suzuki, Takasuke Fukuhara and Keita Matsuno
 488 performed animal experiments.
 489 Yoshitaka Oda, Lei Wang, Masumi Tsuda and Shinya Tanaka performed
 490 histopathological analysis.
 491 Jiri Zahradnik and Gideon Schreiber performed yeast surface display assay.
 492 Sayaka Deguchi and Kazuo Takayama prepared AO, AO-ALI and
 493 airway-on-a-chip systems.
 494 Yuki Yamamoto and Tetsuharu Nagamoto performed generation and provision
 495 of human iPSC-derived airway and alveolar epithelial cells.
 496 Hiroyuki Asakura, Mami Nagashima, Kenji Sadamasu and Kazuhisa Yoshimura
 497 performed viral genome sequencing analysis.
 498 Jumpei Ito performed statistical, modelling, and bioinformatics analyses.
 499 Jumpei Ito, Terumasa Ikeda, Takasuke Fukuhara, Akatsuki Saito, Shinya
 500 Tanaka, Keita Matsuno, Kazuo Takayama and Kei Sato designed the
 501 experiments and interpreted the results.
 502 Jumpei Ito and Kei Sato wrote the original manuscript.
 503 All authors reviewed and proofread the manuscript.
 504 The Genotype to Phenotype Japan (G2P-Japan) Consortium contributed to the
 505 project administration.

507 **Conflict of interest**

508 Yuki Yamamoto and Tetsuharu Nagamoto are founders and shareholders of
 509 HiLung, Inc. Yuki Yamamoto is a co-inventor of patents (PCT/JP2016/057254;
 510 "Method for inducing differentiation of alveolar epithelial cells",
 511 PCT/JP2016/059786, "Method of producing airway epithelial cells"). The other
 512 authors declare that no competing interests exist.

514 **Acknowledgments**

515 We would like to thank all members belonging to The Genotype to Phenotype
 516 Japan (G2P-Japan) Consortium. We thank Dr. Kenzo Tokunaga (National
 517 Institute for Infectious Diseases, Japan) and Dr. Jin Gohda (The University of
 518 Tokyo, Japan) for providing reagents. We also thank National Institute for
 519 Infectious Diseases, Japan for providing clinical isolates of BQ.1.1 (strain
 520 TY41-796-P1; GISAID ID: EPI_ISL_15579783) and BA.2 (strain TY40-385;

521 GISAID ID: EPI_ISL_9595859). We appreciate the technical assistance from
522 The Research Support Center, Research Center for Human Disease Modeling,
523 Kyushu University Graduate School of Medical Sciences. We gratefully
524 acknowledge all data contributors, i.e. the Authors and their Originating
525 laboratories responsible for obtaining the specimens, and their Submitting
526 laboratories for generating the genetic sequence and metadata and sharing via
527 the GISAID Initiative, on which this research is based. The super-computing
528 resource was provided by Human Genome Center at The University of Tokyo.

529 This study was supported in part by AMED SCARDA Japan Initiative
530 for World-leading Vaccine Research and Development Centers "UTOPIA"
531 (JP223fa627001, to Kei Sato), AMED SCARDA Program on R&D of new
532 generation vaccine including new modality application (JP223fa727002, to Kei
533 Sato); AMED Research Program on Emerging and Re-emerging Infectious
534 Diseases (JP21fk0108574, to Hesham Nasser; JP21fk0108481, to Akatsuki
535 Saito; JP21fk0108465, to Akatsuki Saito; JP21fk0108493, to Takasuke
536 Fukuhara; JP22fk0108617 to Takasuke Fukuhara; JP22fk0108146, to Kei Sato;
537 JP21fk0108494 to G2P-Japan Consortium, Keita Matsuno, Shinya Tanaka,
538 Terumasa Ikeda, Takasuke Fukuhara, and Kei Sato; JP21fk0108425, to Kazuo
539 Takayama, Akatsuki Saito and Kei Sato; JP21fk0108432, to Kazuo Takayama,
540 Takasuke Fukuhara and Kei Sato); AMED Research Program on HIV/AIDS
541 (JP22fk0410033, to Akatsuki Saito; JP22fk0410047, to Akatsuki Saito;
542 JP22fk0410055, to Terumasa Ikeda; and JP22fk0410039, to Kei Sato); AMED
543 CRDF Global Grant (JP22jk0210039 to Akatsuki Saito); AMED Japan Program
544 for Infectious Diseases Research and Infrastructure (JP22wm0325009, to
545 Akatsuki Saito; JP22wm0125008 to Keita Matsuno); AMED CREST
546 (JP21gm1610005, to Kazuo Takayama); JST PRESTO (JPMJPR22R1, to
547 Jumpei Ito); JST CREST (JPMJCR20H4, to Kei Sato); JSPS KAKENHI
548 Grant-in-Aid for Scientific Research C (22K07103, to Terumasa Ikeda); JSPS
549 KAKENHI Grant-in-Aid for Scientific Research B (21H02736, to Takasuke
550 Fukuhara); JSPS KAKENHI Grant-in-Aid for Early-Career Scientists (22K16375,
551 to Hesham Nasser; 20K15767, Jumpei Ito); JSPS Core-to-Core Program (A.
552 Advanced Research Networks) (JPJSCCA20190008, Kei Sato); JSPS Research
553 Fellow DC2 (22J11578, to Keiya Uriu); JSPS Leading Initiative for Excellent
554 Young Researchers (LEADER) (to Terumasa Ikeda); World-leading Innovative
555 and Smart Education (WISE) Program 1801 from the Ministry of Education,
556 Culture, Sports, Science and Technology (MEXT) (to Naganori Nao); The Tokyo
557 Biochemical Research Foundation (to Kei Sato); Takeda Science Foundation (to
558 Terumasa Ikeda); Mochida Memorial Foundation for Medical and
559 Pharmaceutical Research (to Terumasa Ikeda); The Naito Foundation (to
560 Terumasa Ikeda); Shin-Nihon Foundation of Advanced Medical Research (to
561 Terumasa Ikeda); Waksman Foundation of Japan (to Terumasa Ikeda); an

intramural grant from Kumamoto University COVID-19 Research Projects (AMABIE) (to Terumasa Ikeda); Ito Foundation Research Grant R4 (to Akatsuki Saito); and the project of National Institute of Virology and Bacteriology, Programme EXCELES, funded by the European Union, Next Generation EU (LX22NPO5103, to Jiri Zahradnik).

Consortia

Hirofumi Sawa^{7,13,14}, Marie Kato¹¹, Zannatul Ferdous¹¹, Hiromi Mouri¹¹, Kenji Shishido¹¹, Naoko Misawa², Izumi Kimura², Lin Pan², Mai Suganami², Mika Chiba², Ryo Yoshimura², Kyoko Yasuda², Keiko Iida², Naomi Ohsumi², Adam P. Strange², Daniel Sauter^{2,30}, So Nakagawa³¹ Jiaqi Wu³¹, Rina Hashimoto¹⁶, Yukio Watanabe¹⁶, Ayaka Sakamoto¹⁶, Naoko Yasuhara¹⁶, Takao Hashiguchi³², Tateki Suzuki³², Kanako Kimura³², Jiei Sasaki³², Yukari Nakajima³², Hisano Yajima³², Kotaro Shirakawa³², Akifumi Takaori-Kondo³², Kayoko Nagata³², Yasuhiro Kazuma³², Ryosuke Nomura³², Yoshihito Horisawa³², Yusuke Tashiro³², Yugo Kawa³², Takashi Irie³³, Ryoko Kawabata³³, Ryo Shimizu⁷, Otowa Takahashi⁷, Kimiko Ichihara⁷, Chihiro Motozono³⁴, Mako Toyoda³⁴, Takamasa Ueno³⁴, Yuki Shibatani⁹, Tomoko Nishiuchi⁹

³⁰University Hospital Tübingen, Tübingen, Germany

³¹Tokai University School of Medicine, Isehara, Japan

³²Kyoto University, Kyoto, Japan

³³Hiroshima University, Hiroshima, Japan

³⁴Kumamoto University, Kumamoto, Japan

587 **Figure legends**

588 **Fig. 1. Phylogenetic and epidemic analyses of the XBB lineage**

589 **a**, Phylogenetic tree of representative sequences from PANGO lineages of
590 interest: BA.1, BA.2, BA.4, BA.5, BA.2.75, BJ.1, and BM.1.1.1, rooted on a B.1.1
591 outgroup (not shown). The recombinant parents of XBB are annotated on the
592 tree as cartoon clades.

593 **b**, Amino acid differences in the S proteins of Omicron lineages.

594 **c**, Nucleotide differences between the consensus sequences of the BJ.1, BM.1
595 (including BM.1.1/BM.1.1.1) lineages and the XBB (including XBB.1) lineage,
596 visualized with snipit (<https://github.com/aineniameh/snipit>).

597 **d**, Maximum likelihood time-calibrated phylogeny of the 5' non-recombinant
598 segment (1–22,920) of the XBB variant (left) and non-calibrated phylogeny of
599 the 3' non-recombinant segment (22,920–29,903) (right). Both trees are rooted
600 on a BA.2 outgroup (not shown).

601 **e**, Ancestral state reconstruction of the circulated regions of viruses. The
602 time-calibrated tree shown in **Fig. 1d, left** is inherited in this analysis. Phylogeny
603 related to XBB is only shown. Black circles on tips indicate samples from India.
604 Branch color indicates the ancestral likelihood of the presence in India. In
605 addition, the ancestral likelihood value for the MRCA of XBB lineages is shown
606 as a pie chart. See also **Extended Data Fig. S1a**.

607 **f**, Relative R_e values for viral lineages in India, assuming a fixed generation time
608 of 2.1 days. The R_e of BA.2 is set at 1. Dot color indicates the posterior mean of
609 the R_e , and an arrow indicate phylogenetic relationship. See also **Extended**
610 **Data Fig. S1b**.

611 **g**, Difference in the circulated regions between BQ.1 and XBB lineages.
612 Estimated lineage frequency as of November 15th, 2022 in each country is
613 shown. Countries with $\geq 50\%$ and $\geq 20\%$ frequencies are annotated for the BQ.1
614 and XBB lineages, respectively.

615 **h**, Relative R_e values for viral lineages, assuming a fixed generation time of 2.1
616 days. The R_e value of BA.5 is set at 1. The posterior (violin), posterior mean (dot),
617 and 95% Bayesian confidential interval (CI; line) are shown. The global average
618 values estimated by a hierarchical Bayesian model²³ are shown. See also
619 **Extended Data Fig. S1c**.

620 **i**, Estimated lineage dynamics in each country where BQ.1 and XBB lineages
621 cocirculated.

622 **Fig. 2. Immune resistance of XBB**

624 Neutralization assays were performed with pseudoviruses harboring the S
625 proteins of BA.2, BA.5, BQ.1.1, BA.2.75 and XBB. The BA.2 S-based derivatives
626 are included in **a and b**. The following sera were used.

627 **a,b**, Convalescent sera from fully vaccinated individuals who had been infected
 628 with BA.2 after full vaccination (9 2-dose vaccinated and 5 3-dose vaccinated. 14
 629 donors in total) (**a**), and BA.5 after full vaccination (2 2-dose vaccinated donors,
 630 17 3-dose vaccinated donors and 1 4-dose vaccinated donors. 20 donors in
 631 total) (**b**).
 632 **c**, Sera from hamsters infected with BA.2 (12 hamsters), BA.5 (12 hamsters),
 633 BQ.1.1 (6 hamsters), BA.2.75 (12 hamsters), and XBB (6 hamsters).
 634 **d**, Antigenic cartography based on the results of neutralization assays using
 635 hamster sera (**Fig. 2c**).
 636 Assays for each serum sample were performed in triplicate to determine the
 637 50% neutralization titer (NT₅₀). Each dot represents one NT₅₀ value, and the
 638 geometric mean and 95% CI are shown. Statistically significant differences were
 639 determined by two-sided Wilcoxon signed-rank tests. The *P* values versus BA.2
 640 (**a**), BA.5 (**b**), or XBB (**c**) are indicated in the panels.
 641 For the BA.2 derivatives (**a and b**), statistically significant differences (*P* < 0.05)
 642 versus BA.2 are indicated with asterisks. Red and blue asterisks, respectively,
 643 indicate decreased and increased NT₅₀s.
 644 The horizontal dashed line indicates the detection limit (120-fold). Information on
 645 the convalescent donors is summarized in **Supplementary Table 4**.

647 **Fig. 3. Virological characteristics of XBB *in vitro***

648 **a**, Binding affinity of the RBD of SARS-CoV-2 S protein to ACE2 by yeast
 649 surface display. The K_D value indicating the binding affinity of the RBD of the
 650 SARS-CoV-2 S protein to soluble ACE2 when expressed on yeast is shown.
 651 **b**, Pseudovirus assay. HOS-ACE2-TMPRSS2 cells were infected with
 652 pseudoviruses bearing each S protein. The amount of input virus was
 653 normalized based on the amount of HIV-1 p24 capsid protein. The percent
 654 infectivity compared to that of the virus pseudotyped with the BA.2 S protein are
 655 shown.
 656 **c**, Fold increase in pseudovirus infectivity based on TMPRSS2 expression.
 657 **d,e**, S-based fusion assay. **d**, S protein expression on the cell surface. The
 658 summarized data are shown. **e**, S-based fusion assay in Calu-3 cells. The
 659 recorded fusion activity (arbitrary units) is shown. The dashed green line
 660 indicates the result of BA.2. The red number in each panel indicates the fold
 661 difference between BA.2 and the derivative tested (XBB in the top left panel) at
 662 24 h post coculture.
 663 **f–m**, Growth kinetics of XBB. Clinical isolates of BA.2, BA.2.75, XBB and Delta
 664 (only in **i,m**) were inoculated into Vero cells (**f**), VeroE6/TMPRSS2 cells (**g**),
 665 Calu-3 cells (**h**), AO-ALI (**i**), iPSC-derived airway epithelial cells (**j**), iPSC-derived
 666 lung epithelial cells (**k**) and an airway-on-a-chip system (**l**). The copy numbers of
 667 viral RNA in the culture supernatant (**f–h**), the apical sides of cultures (**i–k**), and

the top (**l, left**) and bottom (**l, right**) channels of an airway-on-a-chip were routinely quantified by RT-qPCR. In **m**, the percentage of viral RNA load in the bottom channel per top channel at 6 d.p.i. (i.e., % invaded virus from the top channel to the bottom channel) is shown. Assays were performed in triplicate (**a,l,m**) or quadruplicate (**b-k**). The presented data are expressed as the average \pm SD (**a-e**) or SEM (**f-m**). In **a-d,m**, each dot indicates the result of an individual replicate. In **a-d**, the dashed horizontal lines indicate the value of BA.2. In **a-d**, statistically significant differences (*, $P < 0.05$) versus BA.2 were determined by two-sided Student's *t* tests. Red and blue asterisks, respectively, indicate increased and decreased values. In **e-l**, statistically significant differences versus BA.2.75 (**e-k**) or XBB (**l**) across timepoints were determined by multiple regression. In **m**, statistically significant differences versus XBB were determined by two-sided Student's *t* tests. The FWERs calculated using the Holm method (**e-l**) or *P* values (**m**) are indicated in the figures.

Fig. 4. Virological characteristics of XBB *in vivo*

Syrian hamsters were intranasally inoculated with BA.2.75, XBB and Delta. Six hamsters of the same age were intranasally inoculated with saline (uninfected). Six hamsters per group were used to routinely measure the respective parameters (**a**). Four hamsters per group were euthanized at 2 and 5 d.p.i. and used for virological and pathological analysis (**b-e**).

a, Body weight, Penh, and Rpef values of infected hamsters ($n = 6$ per infection group).

b, (Left) Viral RNA loads in the oral swab ($n=6$ per infection group). (Middle and right) Viral RNA loads in the lung hilum (middle) and lung periphery (right) of infected hamsters ($n=4$ per infection group).

c, IHC of the viral N protein in the lungs at 2 d.p.i. (top) and 5 d.p.i. (bottom) of infected hamsters. Representative figures (left, N-positive cells are shown in brown) and the percentage of N-positive cells in whole lung lobes (right, $n=4$ per infection group) are shown. The raw data are shown in **Extended Data Fig. 3**.

d,e, H&E staining of the lungs of infected hamsters. Representative figures are shown in **d**. Uninfected lung alveolar space and bronchioles are also shown. **e**, Histopathological scoring of lung lesions ($n=4$ per infection group). Representative pathological features are reported in our previous studies^{2,5,10,23,25,26}.

In **a-c**, data are presented as the average \pm SEM.

In **a,b,c,e**, statistically significant differences between XBB and other variants across timepoints were determined by multiple regression. In **a**, the 0 d.p.i. data were excluded from the analyses. The FWERs calculated using the Holm method are indicated in the figures.

709 Scale bars, 500 μm (c); 200 μm (d).

710

711 **Supplementary Table 1.** Estimated relative R_e values of XBB-related lineages
712 in India

713

714 **Supplementary Table 2.** Estimated lineage frequencies for BQ.1, XBB other
715 lineages as of November 15, 2022 in each country

716

717 **Supplementary Table 3.** Estimated relative R_e values of viral lineages by a
718 hierarchical Bayesian model

719

720 **Supplementary Tables 4.** Human sera used in this study

721

722 **Supplementary Table 5.** Primers used for the construction of SARS-CoV-2 S
723 expression plasmids

724

725 **Supplementary Table 6.** Summary of unexpected amino acid mutations
726 detected in the working virus stocks

727

728 **Extended Data Fig. 1. Phylogenetic and epidemic analyses of the XBB**
729 **lineage**

730 **a,** Ancestral state reconstruction of the circulated regions of viruses, related to
731 **Fig. 1e.** Unlike **Fig. 1e**, result for the entire of the tree is shown. An asterisk
732 denotes the MRCA node of XBB lineages.

733 **b,** Relative R_e values for viral lineages in India, assuming a fixed generation time
734 of 2.1 days, related to **Fig. 1f.** The R_e of BA.2 is set at 1. The posterior (violin),
735 posterior mean (dot), and 95% Bayesian CI (line) are shown.

736 **c,** Relative R_e values for viral lineages, assuming a fixed generation time of 2.1
737 days, related to **Fig. 1h.** The R_e value of BA.5 is set at 1. The posterior (violin),
738 posterior mean (dot), and 95% Bayesian CI (line) are shown. R_e values for each
739 country where BQ.1 and XBB lineages cocirculated are shown.

740

741 **Extended Data Fig. 2. Fusogenicity of BA.2.75 S**

742 **a,b,** S-based fusion assay. **a,** S protein expression on the cell surface. The
743 summarized data are shown. **b,** S-based fusion assay in Calu-3 cells. The
744 recorded fusion activity (arbitrary units) is shown. The dashed green line
745 indicates the result of BA.2. The red number in each panel indicates the fold
746 difference between BA.2 and the derivative tested (XBB in the top left panel) at
747 24 h post coculture.

748 Assays were performed in triplicate. The presented data are expressed as the
749 average \pm SD. In **a**, each dot indicates the result of an individual replicate, and

the dashed horizontal lines indicate the value of BA.2. Statistically significant differences (*, $P < 0.05$) versus BA.2 were determined by two-sided Student's t tests, and red asterisks indicate increased values. In **b**, statistically significant differences versus BA.2 across timepoints were determined by multiple regression. The FWERs calculated using the Holm method are indicated in the figures.

756

757 **Extended Data Fig. 3. Histological observations in infected hamsters**

758 IHC of the SARS-CoV-2 N protein in the lungs of infected hamsters at 2 d.p.i. (**a**)
 759 and 5 d.p.i. (**b**) (4 hamsters per infection group). In each panel, IHC staining (top)
 760 and the digitalized N-positive area (bottom, indicated in red) are shown. The red
 761 numbers in the bottom panels indicate the percentage of the N-positive area.
 762 Summarized data are shown in **Fig. 4c, right**. Scale bars, 5 mm.

763 **Methods**

764

765 **Ethics statement**

766 All experiments with hamsters were performed in accordance with the Science
767 Council of Japan's Guidelines for the Proper Conduct of Animal Experiments.
768 The protocols were approved by the Institutional Animal Care and Use
769 Committee of National University Corporation Hokkaido University (approval ID:
770 20-0123 and 20-0060). All protocols involving specimens from human subjects
771 recruited at Interpark Kuramochi Clinic was reviewed and approved by the
772 Institutional Review Board of Interpark Kuramochi Clinic (approval ID:
773 G2021-004). All human subjects provided written informed consent. All protocols
774 for the use of human specimens were reviewed and approved by the Institutional
775 Review Boards of The Institute of Medical Science, The University of Tokyo
776 (approval IDs: 2021-1-0416 and 2021-18-0617) and University of Miyazaki
777 (approval ID: O-1021).

778

779 **Human serum collection**

780 Convalescent sera were collected from fully vaccinated individuals who had
781 been infected with BA.2 (9 2-dose vaccinated and 5 3-dose vaccinated; 11–61
782 days after testing. n=14 in total; average age: 47 years, range: 24–84 years,
783 64% male) (**Fig. 2a**), and fully vaccinated individuals who had been infected with
784 BA.5 (2 2-dose vaccinated, 17 3-dose vaccinated and 1 4-dose vaccinated;
785 10–23 days after testing. n=20 in total; average age: 51 years, range: 25–73
786 years, 45% male) (**Fig. 2b**). The SARS-CoV-2 variants were identified as
787 previously described^{5,10,23}. Sera were inactivated at 56°C for 30 minutes and
788 stored at –80°C until use. The details of the convalescent sera are summarized
789 in **Supplementary Table 4**.

790

791 **Cell culture**

792 HEK293T cells (a human embryonic kidney cell line; ATCC, CRL-3216),
793 HEK293 cells (a human embryonic kidney cell line; ATCC, CRL-1573) and
794 HOS-ACE2/TMPRSS2 cells (HOS cells stably expressing human ACE2 and
795 TMPRSS2)^{35,36} were maintained in DMEM (high glucose) (Sigma-Aldrich, Cat#
796 6429-500ML) containing 10% fetal bovine serum (FBS, Sigma-Aldrich Cat#
797 172012-500ML) and 1% penicillin–streptomycin (PS) (Sigma-Aldrich, Cat#
798 P4333-100ML). HEK293-ACE2 cells (HEK293 cells stably expressing human
799 ACE2)²⁴ were maintained in DMEM (high glucose) containing 10% FBS, 1 µg/ml
800 puromycin (InvivoGen, Cat# ant-pr-1) and 1% PS. HEK293-ACE2/TMPRSS2
801 cells (HEK293 cells stably expressing human ACE2 and TMPRSS2)²⁴ were
802 maintained in DMEM (high glucose) containing 10% FBS, 1 µg/ml puromycin,
803 200 µg/ml hygromycin (Nacalai Tesque, Cat# 09287-84) and 1% PS. Vero cells

[an African green monkey (*Chlorocebus sabaeus*) kidney cell line; JCRB Cell Bank, JCRB0111] were maintained in Eagle's minimum essential medium (EMEM) (Sigma-Aldrich, Cat# M4655-500ML) containing 10% FBS and 1% PS. VeroE6/TMPRSS2 cells (VeroE6 cells stably expressing human TMPRSS2; JCRB Cell Bank, JCRB1819)³⁷ were maintained in DMEM (low glucose) (Wako, Cat# 041-29775) containing 10% FBS, G418 (1 mg/ml; Nacalai Tesque, Cat# G8168-10ML) and 1% PS. Calu-3 cells (ATCC, HTB-55) were maintained in Eagle's minimum essential medium (EMEM) (Sigma-Aldrich, Cat# M4655-500ML) containing 10% FBS and 1% PS. Calu-3/DSP₁₋₇ cells (Calu-3 cells stably expressing DSP₁₋₇)³⁸ were maintained in EMEM (Wako, Cat# 056-08385) containing 20% FBS and 1% PS. Human airway and lung epithelial cells derived from human induced pluripotent stem cells (iPSCs) were manufactured according to established protocols as described below (see "Preparation of human airway and lung epithelial cells from human iPSCs" section) and provided by HiLung Inc. AO-ALI model was generated according to established protocols as described below (see "AO-ALI model" section).

820

821 **Viral genome sequencing**

822 Viral genome sequencing was performed as previously described⁵. Briefly, the
823 virus sequences were verified by viral RNA-sequencing analysis. Viral RNA was
824 extracted using a QIAamp viral RNA mini kit (Qiagen, Cat# 52906). The
825 sequencing library employed for total RNA sequencing was prepared using the
826 NEBNext Ultra RNA Library Prep Kit for Illumina (New England Biolabs, Cat#
827 E7530). Paired-end 76-bp sequencing was performed using a MiSeq system
828 (Illumina) with MiSeq reagent kit v3 (Illumina, Cat# MS-102-3001). Sequencing
829 reads were trimmed using fastp v0.21.0 (ref.³⁹) and subsequently mapped to the
830 viral genome sequences of a lineage B isolate (strain Wuhan-Hu-1; GenBank
831 accession number: NC_045512.2)³⁷ using BWA-MEM v0.7.17 (ref.⁴⁰). Variant
832 calling, filtering, and annotation were performed using SAMtools v1.9 (ref.⁴¹) and
833 snpEff v5.0e⁴².

834

835 **Recombination analysis**

836 As of October 3, 2022, we retrieved a total of 562 sequences satisfying the
837 following criteria from the GISAID database (<https://gisaid.org/>): i) human hosts,
838 ii) collected after 2022, iii) with length greater than 28,000 base pairs, and iv)
839 with PANGO lineage designation BJ.1, BM.1, XBB and all their descendants. To
840 ensure that PANGO lineage definitions in our dataset's metadata included the
841 latest circulating lineages, the GISAID metadata were downloaded again on
842 October 15, 2022, and the PANGO lineages of our sequences were updated
843 accordingly. Sequences were aligned to the reference Wuhan-Hu-1 genome
844 (GenBank Accession no. NC_045512.2) and then converted to a multiple

sequence alignment using the 'global_profile_alignment.sh' script from the SARS-CoV-2 global phylogeny pipeline⁴³, utilizing MAFFT⁴⁴. A number of recombination detection methods were performed on the resulting alignment using the Recombination Detection Program (RDP) v.5.21 (ref.¹⁹), specifically: RDP⁴⁵, GENECONV⁴⁶, Chimaera⁴⁷, MaxChi⁴⁸, 3seq⁴⁹, BootScan⁵⁰ and SiScan⁵¹. Sequences were assumed to be linear, only recombination events detected consistently by more than 3 independent methods were retrieved and potential false positives were excluded from the final output of RDP5.

Phylogenetic analyses

To reconstruct the overall relatedness of the XBB parent lineages BJ.1 and BM.1.1.1 to the other Omicron variants (**Fig. 1a**) we retrieved 100 random sequences from each Omicron PANGO lineages: BA.1, BA.2, BA.4 and BA.5 and 20 random sequences from each younger lineage: BQ.1.1, BA.2.75, BJ.1, and BM.1.1.1. Sequence EPI_ISL_466615 was also added as an outgroup, representing the oldest isolate of B.1.1 obtained in the UK. The sequences were aligned to the reference Wuhan-Hu-1 genome (NC_045512.2) and then converted to a multiple sequence alignment using the 'global_profile_alignment.sh' script from the SARS-CoV-2 global phylogeny pipeline⁴³ utilizing MAFFT⁴⁴. Fasttree v.2.1 (ref.⁵²) was used to infer the phylogeny for the nucleotide alignment under a GTR substitution model (option -gtr).

For inferring the phylogenies of each non-recombinant segment of the XBB variant, we first split the alignment used for the recombination analysis above at genome position 22,920 (the breakpoint inferred by RDP5). Due to the lack of many informative sites of the 3' end shorter non-recombinant alignment, two quality filtering steps were implemented: i) the 3' end of the alignment was trimmed up to the position where none of the sequences had 3' end gaps and ii) all sequences with Ns were removed, leading to a reduced alignment of 370 sequences. BA.2 sequence EPI_ISL_10926749 was added to the alignments as an outgroup. Iqtree2 v2.1.3 (ref.⁵³) was used for making a phylogenetic for each non-recombinant alignment. The TIM2+F+I substitution model was used for both trees as selected by the '-m TEST' of iqtree and node support was assessed by performing 1000 ultrafast bootstrap replicates.

Both phylogenies were manually inspected for the presence of temporal signal using TempEst v1.5.3 (ref.⁵⁴). The 3' end non-recombinant segment's phylogeny did not have enough substitutions for a root-to-tip regression to be inferred, hence we proceeded with tip-dating analysis only for the 5' end, longer segment. The 5' end phylogeny was manually rooted to the BA.2 outgroup branch with FigTree [<https://github.com/rambaut/figtree/>] and TreeTime v.0.8.1 (ref.⁵⁵) was used for the time-calibration (maintaining the rooting with the

–keep-root option). The substitution rate inferred by the root-to-tip regression and used for the tree calibration was 1.10E-3 substitutions per site per year, consistent with the accepted rate for SARS-CoV-2 (ref.⁵⁶). Two terminal branches with dates not matching the root-to-tip regression were manually removed from the phylogeny.

To infer the emergence region of XBB, we performed a discrete ancestral state reconstruction analysis utilizing a Markov model. In this analysis, the time-calibrated phylogenetic tree of the 5' non-recombinant segment (1–22,920) (shown in **Fig. 1d, left**) was used. First, based on the sampled (or circulating) region of each virus in the tree, we defined the discrete state of the circulating region for each viral sequence according to the following rules: For samples from India, Bangladesh, and Singapore, the states “India”, “Bangladesh”, and “Singapore” were assigned respectively. For samples from the other Asian countries, “Other Asian countries” was assigned. For samples from European and Northern American countries, “European countries” and “Northern American countries” were assigned, respectively. For samples from the other regions, “Other regions” was assigned. We subsequently inferred the ancestral likelihoods of the seven states (i.e., circulating regions) for each internal node of the tree using the `asr_mk_model` function in the `castor` package⁵⁷. In the tree shown in **Fig. 1e and Extended Data Fig. 1b**, we mapped the ancestral likelihood of the state “India” to the tree. The analyses above were performed on R v.4.2.1.

Epidemic dynamics analyses

We modeled the epidemic dynamics of viral lineages based on the viral genomic surveillance data deposited in the GISAID database (<https://www.gisaid.org/>). In the present study, we performed three types of analyses: i) The estimation of the relative R_e for lineages related to XBB in India (shown in **Fig. 1f and Extended Data Fig. 1c**), ii) The estimation of the epidemic frequencies of XBB and BQ.1 lineages in each country as of November 15, 2022 (shown in **Fig. 1g**), and iii) The estimation of the global and country-specific R_e value of XBB and BQ.1 lineages in the countries where these variants circulated (**Fig. 1h,i and Extended Data Fig. 1d**). For the three analyses, the metadata of viral sequences downloaded from the GISAID database on December 1st, 2022 was used. We excluded the sequence records with the following features: i) a lack of collection date information; ii) sampling in animals other than humans; iii) sampling by quarantine; or iv) without the PANGO lineage information.

To estimate the relative R_e for lineages related to XBB in India, we analyzed the records for samples from India from June 1, 2022 to November 15, 2022. We removed records with >5% undetermined (N) nucleotide sequences from the dataset. We first simplified the viral lineage classification based on the

PANGO lineage. We renamed the sublineages of BA.5 as BA.5, and subsequently, we removed the BA.5 sequences harboring any of the convergent S substitutions, S:R346X, S:K444X, and S:N460X from our dataset in order to exclude the sequences belonging to the recent BA.5 sublineages exhibiting particularly higher R_e such as BQ.1.1 (ref.²). Also, we removed the sequences of BA.2.75 harboring any of the convergent S substitutions, S:R346X, S:K444X, S:N460X, and S:F486X. Furthermore, since a part of BA.2.10.1 sequences harbor XBB-characteristic substitutions (S:V83A, S:F486S, and S:F490S) probably due to the misclassification of XBB, we removed the sequences of BA.2.10.1 harboring these XBB-characteristic substitutions. According to the modified viral lineages, we extracted records for viral lineages of interest: BA.2, BA.5, BA.2.75, BM.1, BM1.1, BM.1.1.1, BA.2.10, BJ.1, XBB, and XBB.1. Subsequently, we counted the daily frequency of each viral lineage. Relative R_e value for each viral lineage was estimated according to the Bayesian multinomial logistic model, described in our previous study⁵. Briefly, we estimated the logistic slope parameter β_l for each viral lineage using the model and then calculated relative R_e for each lineage r_l as $r_l = \exp(\gamma\beta_l)$ where γ is the average viral generation time (2.1 days) (http://sonorouschocolate.com/covid19/index.php?title=Estimating_Generation_Time_Of_Omicron). Parameter estimation was performed via the MCMC approach implemented in CmdStan v2.30.1 (<https://mc-stan.org>) with CmdStanr v0.5.3 (<https://mc-stan.org/cmdstanr/>). Four independent MCMC chains were run with 500 and 1,000 steps in the warmup and sampling iterations, respectively. We confirmed that all estimated parameters showed <1.01 R-hat convergence diagnostic values and >200 effective sampling size values, indicating that the MCMC runs were successfully convergent. Information on the estimated parameters is summarized in **Supplementary Table 1**.

To estimate the epidemic frequencies of XBB and BQ.1 lineages in each country as of November 15, 2022, we analyzed the records for viral samples collected from August 1, 2022 to November 15th, 2022. In data for each country, we counted the daily lineage frequency of BQ.1 (including its decedent sublineages), XBB (including its decedent sublineages), and the other SARS-CoV-2 lineages (referred to as “Other lineages”). We analyzed the data only for countries with a total of ≥ 1000 samples or ≥ 50 samples of either the BQ.1 or XBB lineages. In this criterion, 56 countries remained. Subsequently, we fitted the multinomial logistic model described in the paragraph above to the daily lineage frequency data of each country separately, and the epidemic frequency of each viral lineage as of November 15, 2022 in each country was estimated. If the data for November 15, 2022 in a particular country are not available, the lineage frequencies at the latest date in the country were used instead. The estimated lineage frequencies for BQ.1 and XBB in each country

were shown on the global map using The R library maps v3.4.1 (<https://cran.r-project.org/web/packages/maps/index.html>). Information on the estimated lineage frequencies is summarized in **Supplementary Table 2**.

To estimate the global average and country-specific R_e values for BQ.1 and XBB lineages, we analyzed the sequence records for viral samples collected from August 1, 2022 to November 15, 2022. We defined the sequences of BQ.1 (including its sublineages) harboring S:R346T as BQ.1.1 and the other BQ.1 sequences as BQ.1. Similarly, the sequences of XBB (including its sublineages) harboring S:G252V as XBB and the other XBB sequences as XBB. Subsequently, we extracted the sequence records of BQ.1, BQ.1.1, XBB, and XBB.1 in addition to BA.5 (including its sublineages) and BA.2.75 (including its sublineages), which are predominant lineages before the BQ.1 and XBB emergencies. Next, we counted the daily frequency of the lineages above in each country. We analyzed counties with a total of ≥ 1000 samples and ≥ 200 samples of either the BQ.1, BQ.1.1, XBB, or XBB.1 lineages. In this criterion, 11 countries (Australia, Austria, Denmark, India, Indonesia, Israel, Malaysia, Peru, Singapore, the UK, and the USA) remained. To estimate the global average R_e values of the lineages above, we employed a hierarchal Bayesian multinomial logistic model, which we established in our previous studies^{10,23}. Briefly, this hierarchal model can estimate the global average and country-specific R_e values of lineages of interest simultaneously according to the daily lineage frequency data from multiple countries. The relative R_e of each viral lineage l in each county s (r_{ls}) was calculated according to the country-specific slope parameter, β_{ls} , as $r_{ls} = \exp(\gamma\beta_{ls})$ where γ is the average viral generation time (2.1 days). Similarly, the global average relative R_e of each viral lineage was calculated according to the global average slope parameter, β_l , as $r_l = \exp(\gamma\beta_l)$. For parameter estimation, the global average intercept and slope parameters of the BA.5 variant were fixed at 0. Consequently, the relative R_e of BA.5 was fixed at 1, and those of the other lineages were estimated relative to that of BA.5. Parameter estimation was performed via the MCMC approach implemented in CmdStan v2.30.1 (<https://mc-stan.org>) with CmdStanr v0.5.3 (<https://mc-stan.org/cmdstanr/>). Four independent MCMC chains were run with 500 and 2,000 steps in the warmup and sampling iterations, respectively. We confirmed that all estimated parameters showed <1.01 R-hat convergence diagnostic values and >200 effective sampling size values, indicating that the MCMC runs were successfully convergent. Information on the estimated parameters is summarized in **Supplementary Table 3**.

Plasmid construction

Plasmids expressing the codon-optimized SARS-CoV-2 S proteins of B.1.1 (the parental D614G-bearing variant), BA.2 and BA.5, BQ.1.1 and BA.2.75 were

prepared in our previous studies^{2,5,10,23,24,58}. Plasmids expressing the codon-optimized S proteins of XBB and BA.2 S-based derivatives were generated by site-directed overlap extension PCR using the primers listed in **Supplementary Table 5**. The resulting PCR fragment was digested with KpnI (New England Biolabs, Cat# R0142S) and NotI (New England Biolabs, Cat# R1089S) and inserted into the corresponding site of the pCAGGS vector⁵⁹. Nucleotide sequences were determined by DNA sequencing services (Eurofins), and the sequence data were analyzed by Sequencher v5.1 software (Gene Codes Corporation).

Neutralization assay

Pseudoviruses were prepared as previously described^{2,5,10,23,26,28,31,32,36,38,58,60}. Briefly, lentivirus (HIV-1)-based, luciferase-expressing reporter viruses were pseudotyped with SARS-CoV-2 S proteins. HEK293T cells (1,000,000 cells) were cotransfected with 1 µg psPAX2-IN/HiBiT³⁵, 1 µg pWPI-Luc2³⁵, and 500 ng plasmids expressing parental S or its derivatives using PEI Max (Polysciences, Cat# 24765-1) according to the manufacturer's protocol. Two days posttransfection, the culture supernatants were harvested and centrifuged. The pseudoviruses were stored at -80°C until use.

The neutralization assay (**Fig. 2**) was prepared as previously described^{2,5,10,23,26,28,31,32,36,38,58,60}. Briefly, the SARS-CoV-2 S pseudoviruses (counting ~20,000 relative light units) were incubated with serially diluted (120-fold to 87,480-fold dilution at the final concentration) heat-inactivated sera at 37°C for 1 hour. Pseudoviruses without sera were included as controls. Then, a 40 µl mixture of pseudovirus and serum/antibody was added to HOS-ACE2/TMPRSS2 cells (10,000 cells/50 µl) in a 96-well white plate. At 2 d.p.i., the infected cells were lysed with a One-Glo luciferase assay system (Promega, Cat# E6130), a Bright-Glo luciferase assay system (Promega, Cat# E2650), or a britelite plus Reporter Gene Assay System (PerkinElmer, Cat# 6111 6066769), and the luminescent signal was measured using a GloMax explorer multimode microplate reader 3500 (Promega) or CentroXS3 (Berthold Technologies). The assay of each serum sample was performed in triplicate, and the 50% neutralization titer (NT₅₀) was calculated using Prism 9 software v9.1.1 (GraphPad Software).

SARS-CoV-2 preparation and titration

The working virus stocks of SARS-CoV-2 were prepared and titrated as previously described^{2,5,10,23-26,28,30,61}. In this study, clinical isolates of B.1.1 (strain TKYE610670; GISAID ID: EPI_ISL_479681)²⁵, Delta (B.1.617.2, strain TKYTK1734; GISAID ID: EPI_ISL_2378732)²⁶, BA.2 (strain TY40-385; GISAID ID: EPI_ISL_9595859)⁵, BA.5 (strain TKYS14631; GISAID ID:

1050 EPI_ISL_12812500)^{10,30}, BA.2.75 (strain TY41-716; GISAID ID:
1051 EPI_ISL_13969765)¹⁰ and XBB (strain TY41-795; GISAID ID:
1052 EPI_ISL_15669344) were used. In brief, 20 µl of the seed virus was inoculated
1053 into VeroE6/TMPRSS2 cells (5,000,000 cells in a T-75 flask). One h.p.i., the
1054 culture medium was replaced with DMEM (low glucose) (Wako, Cat#
1055 041-29775) containing 2% FBS and 1% PS. At 3 d.p.i., the culture medium was
1056 harvested and centrifuged, and the supernatants were collected as the working
1057 virus stock.

1058 The titer of the prepared working virus was measured as the 50%
1059 tissue culture infectious dose (TCID₅₀). Briefly, one day before infection,
1060 VeroE6/TMPRSS2 cells (10,000 cells) were seeded into a 96-well plate. Serially
1061 diluted virus stocks were inoculated into the cells and incubated at 37°C for 4
1062 days. The cells were observed under a microscope to judge the CPE
1063 appearance. The value of TCID₅₀/ml was calculated with the Reed–Muench
1064 method⁶².

1065 For verification of the sequences of SARS-CoV-2 working viruses, viral
1066 RNA was extracted from the working viruses using a QIAamp viral RNA mini kit
1067 (Qiagen, Cat# 52906) and viral genome sequences were analyzed as described
1068 above (see "Viral genome sequencing" section). Information on the unexpected
1069 substitutions detected is summarized in **Supplementary Table S6**, and the raw
1070 data are deposited in the Sequence Read Archive (accession ID: PRJDB14899).

1071

1072 **Yeast surface display**

1073 Yeast surface display (**Fig. 3a**) was performed as previously described^{2,10,21,22}.
1074 Briefly, the RBD genes ["construct 3" in ref.²², covering residues 330–528] in the
1075 pJYDC1 plasmid were cloned by restriction enzyme-free cloning and
1076 transformed into the EBY100 *Saccharomyces cerevisiae*. The primers are listed
1077 in **Supplementary Table S5**. The expression media 1/9 (ref.⁶³) was inoculated
1078 (OD 1) by overnight (220 rpm, 30°C, SD-CAA media) grown culture, followed by
1079 cultivation for 24 hours at 20°C. The medium was supplemented with 10 mM
1080 DMSO solubilized bilirubin (Sigma-Aldrich, Cat# 14370-1G) for expression
1081 cocultivation labeling [pJYDC1, eUnaG2 reporter holo-form formation,
1082 green/yellow fluorescence (excitation at 498 nm, emission at 527 nm)]. Cells
1083 (100 µl aliquots) were collected by centrifugation (3000 g, 3 minutes), washed in
1084 ice-cold PBSB buffer (PBS with 1 mg/ml BSA), and resuspended in an analysis
1085 solution with a series of CF®640R succinimidyl ester labeled (Biotium, Cat#
1086 92108) ACE2 peptidase domain (residues 18–740) concentrations. The
1087 peptidase domain of wild-type ACE2 and ACE2 N90Q were produced and
1088 purified as previously described²². The reaction volume was adjusted (1–100 ml)
1089 to avoid the ligand depletion effect, and the suspension was incubated overnight
1090 in a rotator shaker (10 rpm, 4°C). Incubated samples were washed with PBSB

1091 buffer, transferred into a 96-well plate (Thermo Fisher Scientific, Cat# 268200),
1092 and analyzed by a CytoFLEX S Flow Cytometer (Beckman Coulter, USA, Cat#.
1093 N0-V4-B2-Y4) with the gating strategy described previously²². The eUnaG2
1094 signals were compensated by CytExpert software (Beckman Coulter). The mean
1095 binding signal (FL4-A) values of RBD-expressing cells, subtracted by signals of
1096 nonexpressing populations, were subjected to the determination of the
1097 dissociation constant K_D , Y_D by a noncooperative Hill equation fitted by nonlinear
1098 least-squares regression using Python v3.7 fitted together with two additional
1099 parameters describing the titration curve²².

1100

1101 **Pseudovirus infection**

1102 Pseudovirus infection (**Fig. 3b**) was performed as previously
1103 described^{2,5,10,23,26,28,31,32,36,38,58,60}. Briefly, the amount of pseudoviruses prepared
1104 was quantified by the HiBiT assay using a Nano Glo HiBiT lytic detection system
1105 (Promega, Cat# N3040) as previously described^{35,64}. For measurement of
1106 pseudovirus infectivity, the same amount of pseudoviruses (normalized to the
1107 HiBiT value, which indicates the amount of HIV-1 p24 antigen) was inoculated
1108 into HOS-ACE2/TMPRSS2 cells, HEK293-ACE2 cells or
1109 HEK293-ACE2/TMPRSS2 cells and viral infectivity was measured as described
1110 above (see “Neutralization assay” section). For analysis of the effect of
1111 TMPRSS2 on pseudovirus infectivity (**Fig. 3c**), the fold change of the values of
1112 HEK293-ACE2/TMPRSS2 to HEK293-ACE2 was calculated.

1113

1114 **SARS-CoV-2 S-based fusion assay**

1115 A SARS-CoV-2 S-based fusion assay (**Fig. 3d,e**) was performed as previously
1116 described^{2,5,10,23-28}. Briefly, on day 1, effector cells (i.e., S-expressing cells) and
1117 target cells (Calu-3/DSP₁₋₇ cells) were prepared at a density of $0.6\text{--}0.8 \times 10^6$
1118 cells in a 6-well plate. On day 2, for the preparation of effector cells, HEK293
1119 cells were cotransfected with the S expression plasmids (400 ng) and pDSP₈₋₁₁
1120 (ref.⁶⁵) (400 ng) using TransIT-LT1 (Takara, Cat# MIR2300). On day 3 (24 hours
1121 posttransfection), 16,000 effector cells were detached and reseeded into a
1122 96-well black plate (PerkinElmer, Cat# 6005225), and target cells were reseeded
1123 at a density of 1,000,000 cells/2 ml/well in 6-well plates. On day 4 (48 hours
1124 posttransfection), target cells were incubated with EnduRen live cell substrate
1125 (Promega, Cat# E6481) for 3 hours and then detached, and 32,000 target cells
1126 were added to a 96-well plate with effector cells. *Renilla* luciferase activity was
1127 measured at the indicated time points using Centro XS3 LB960 (Berthold
1128 Technologies). For measurement of the surface expression level of the S protein,
1129 effector cells were stained with rabbit anti-SARS-CoV-2 S S1/S2 polyclonal
1130 antibody (Thermo Fisher Scientific, Cat# PA5-112048, 1:100). Normal rabbit IgG
1131 (Southern Biotech, Cat# 0111-01, 1:100) was used as a negative control, and

1132 APC-conjugated goat anti-rabbit IgG polyclonal antibody (Jackson
1133 ImmunoResearch, Cat# 111-136-144, 1:50) was used as a secondary antibody.
1134 The surface expression level of S proteins (**Fig. 3d**) was measured using a
1135 FACS Canto II (BD Biosciences) and the data were analyzed using FlowJo
1136 software v10.7.1 (BD Biosciences). For calculation of fusion activity, *Renilla*
1137 luciferase activity was normalized to the MFI of surface S proteins. The
1138 normalized value (i.e., *Renilla* luciferase activity per the surface S MFI) is shown
1139 as fusion activity.

1140

1141 **AO-ALI model**

1142 An airway organoid (AO) model was generated according to our previous
1143 report^{2,10,29,30}. Briefly, normal human bronchial epithelial cells (NHBEs, Cat#
1144 CC-2540, Lonza) were used to generate AOs. NHBEs were suspended in 10
1145 mg/ml cold Matrigel growth factor reduced basement membrane matrix (Corning,
1146 Cat# 354230). Fifty microliters of cell suspension were solidified on prewarmed
1147 cell culture-treated multiple dishes (24-well plates; Thermo Fisher Scientific,
1148 Cat# 142475) at 37°C for 10 min, and then, 500 µl of expansion medium was
1149 added to each well. AOs were cultured with AO expansion medium for 10 days.
1150 For maturation of the AOs, expanded AOs were cultured with AO differentiation
1151 medium for 5 days.

1152 The AO-ALI model (**Fig. 3i**) was generated according to our previous
1153 report^{10,66}. For generation of AO-ALI, expanding AOs were dissociated into
1154 single cells, and then were seeded into Transwell inserts (Corning, Cat# 3413) in
1155 a 24-well plate. AO-ALI was cultured with AO differentiation medium for 5 days
1156 to promote their maturation. AO-ALI was infected with SARS-CoV-2 from the
1157 apical side.

1158

1159 **Preparation of human airway and lung epithelial cells from human iPSCs**

1160 The air-liquid interface culture of airway and lung epithelial cells (**Fig. 3j,k**) was
1161 differentiated from human iPSC-derived lung progenitor cells as previously
1162 described^{5,10,30,67-69}. Briefly, lung progenitor cells were induced stepwise from
1163 human iPSCs according to a 21-day and 4-step protocol⁶⁷. At day 21, lung
1164 progenitor cells were isolated with the specific surface antigen carboxypeptidase
1165 M and seeded onto the upper chamber of a 24-well Cell Culture Insert (Falcon,
1166 #353104), followed by 28-day and 7-day differentiation of airway and lung
1167 epithelial cells, respectively. Alveolar differentiation medium with
1168 dexamethasone (Sigma-Aldrich, Cat# D4902), KGF (PeproTech, Cat# 100-19),
1169 8-Br-cAMP (Biolog, Cat# B007), 3-isobutyl 1-methylxanthine (IBMX) (Fujifilm
1170 Wako, Cat# 095-03413), CHIR99021 (Axon Medchem, Cat# 1386), and
1171 SB431542 (Fujifilm Wako, Cat# 198-16543) was used for the induction of lung
1172 epithelial cells. PneumaCult ALI (STEMCELL Technologies, Cat# ST-05001)

1173 with heparin (Nacalai Tesque, Cat# 17513-96) and Y-27632 (LC Laboratories,
1174 Cat# Y-5301) hydrocortisone (Sigma-Aldrich, Cat# H0135) was used for
1175 induction of airway epithelial cells.

1176

1177 **Airway-on-a-chips**

1178 Airway-on-a-chips (**Fig. 3l,m**) were prepared as previously described^{2,10,29,30}.
1179 Human lung microvascular endothelial cells (HMVEC-L) were obtained from
1180 Lonza (Cat# CC-2527) and cultured with EGM-2-MV medium (Lonza, Cat#
1181 CC-3202). For preparation of the airway-on-a-chip, first, the bottom channel of a
1182 polydimethylsiloxane (PDMS) device was precoated with fibronectin (3 µg/ml,
1183 Sigma-Aldrich, Cat# F1141). The microfluidic device was generated according to
1184 our previous report⁷⁰. HMVEC-L cells were suspended at 5,000,000 cells/ml in
1185 EGM2-MV medium. Then, 10 µl of suspension medium was injected into the
1186 fibronectin-coated bottom channel of the PDMS device. Then, the PDMS device
1187 was turned upside down and incubated. After 1 hour, the device was turned over,
1188 and the EGM2-MV medium was added into the bottom channel. After 4 days,
1189 AOs were dissociated and seeded into the top channel. AOs were generated
1190 according to our previous report⁶⁶. AOs were dissociated into single cells and
1191 then suspended at 5,000,000 cells/ml in the AO differentiation medium. Ten
1192 microliter suspension medium was injected into the top channel. After 1 hour, the
1193 AO differentiation medium was added to the top channel. In the infection
1194 experiments (**Fig. 3l,m**), the AO differentiation medium containing either BA.2,
1195 BA.2.75, XBB or Delta isolate (500 TCID₅₀) was inoculated into the top channel.
1196 At 2 h.p.i., the top and bottom channels were washed and cultured with AO
1197 differentiation and EGM2-MV medium, respectively. The culture supernatants
1198 were collected, and viral RNA was quantified using RT-qPCR (see “RT-qPCR”
1199 section above).

1200

1201 **Microfluidic device**

1202 A microfluidic device was generated according to our previous report^{10,70}. Briefly,
1203 the microfluidic device consisted of two layers of microchannels separated by a
1204 semipermeable membrane. The microchannel layers were fabricated from
1205 PDMS using a soft lithographic method. PDMS prepolymer (Dow Corning, Cat#
1206 SYLGARD 184) at a base to curing agent ratio of 10:1 was cast against a mold
1207 composed of SU-8 2150 (MicroChem, Cat# SU-8 2150) patterns formed on a
1208 silicon wafer. The cross-sectional size of the microchannels was 1 mm in width
1209 and 330 µm in height. Access holes were punched through the PDMS using a
1210 6-mm biopsy punch (Kai Corporation, Cat# BP-L60K) to introduce solutions into
1211 the microchannels. Two PDMS layers were bonded to a PET membrane
1212 containing 3.0-µm pores (Falcon, Cat# 353091) using a thin layer of liquid PDMS
1213 prepolymer as the mortar. PDMS prepolymer was spin-coated (4000 rpm for 60

sec) onto a glass slide. Subsequently, both the top and bottom channel layers were placed on the glass slide to transfer the thin layer of PDMS prepolymer onto the embossed PDMS surfaces. The membrane was then placed onto the bottom layer and sandwiched with the top layer. The combined layers were left at room temperature for 1 day to remove air bubbles and then placed in an oven at 60°C overnight to cure the PDMS glue. The PDMS devices were sterilized by placing them under UV light for 1 hour before the cell culture.

1221

1222 **SARS-CoV-2 infection**

1223 One day before infection, Vero cells (10,000 cells), VeroE6/TMPRSS2 cells
1224 (10,000 cells) and Calu-3 cells (10,000 cells) were seeded into a 96-well plate.
1225 SARS-CoV-2 [1,000 TCID₅₀ for Vero cells (**Fig. 3f**); 100 TCID₅₀ for
1226 VeroE6/TMPRSS2 cells (**Fig. 3g**) and Calu-3 cells (**Fig. 3h**)] was inoculated and
1227 incubated at 37°C for 1 hour. The infected cells were washed, and 180 µl of
1228 culture medium was added. The culture supernatant (10 µl) was harvested at the
1229 indicated timepoints and used for RT-qPCR to quantify the viral RNA copy
1230 number (see “RT-qPCR” section below). In the infection experiments using
1231 AO-ALI (**Fig. 3i**), human iPSC-derived airway and lung epithelial cells (**Fig. 3j,k**),
1232 working viruses were diluted with Opti-MEM (Thermo Fisher Scientific, Cat#
1233 11058021). The diluted viruses (1,000 TCID₅₀ in 100 µl) were inoculated onto
1234 the apical side of the culture and incubated at 37°C for 1 hour. The
1235 inoculated viruses were removed and washed twice with Opti-MEM. For
1236 collection of the viruses, 100 µl Opti-MEM was applied onto the apical side of
1237 the culture and incubated at 37°C for 10 minutes. The Opti-MEM was
1238 collected and used for RT-qPCR to quantify the viral RNA copy number (see
1239 “RT-qPCR” section below). The infection experiments using an airway-on-a-chip
1240 system (**Fig. 3l,m**) were performed as described above (see “Airway-on-a-chips”
1241 section).

1242

1243 **RT-qPCR**

1244 RT-qPCR was performed as previously described^{2,5,10,23-26,28,30,61}. Briefly, 5 µl
1245 culture supernatant was mixed with 5 µl of 2 × RNA lysis buffer [2% Triton X-100
1246 (Nacalai Tesque, Cat# 35501-15), 50 mM KCl, 100 mM Tris-HCl (pH 7.4), 40%
1247 glycerol, 0.8 U/µl recombinant RNase inhibitor (Takara, Cat# 2313B)] and
1248 incubated at room temperature for 10 min. RNase-free water (90 µl) was added,
1249 and the diluted sample (2.5 µl) was used as the template for real-time RT-PCR
1250 performed according to the manufacturer’s protocol using One Step TB Green
1251 PrimeScript PLUS RT-PCR kit (Takara, Cat# RR096A) and the following
1252 primers: Forward *N*, 5'-AGC CTC TTC TCG TTC CTC ATC AC-3'; and Reverse
1253 *N*, 5'-CCG CCA TTG CCA GCC ATT C-3'. The viral RNA copy number was
1254 standardized with a SARS-CoV-2 direct detection RT-qPCR kit (Takara, Cat#

RC300A). Fluorescent signals were acquired using a QuantStudio 1 Real-Time PCR system (Thermo Fisher Scientific), QuantStudio 3 Real-Time PCR system (Thermo Fisher Scientific), QuantStudio 5 Real-Time PCR system (Thermo Fisher Scientific), StepOne Plus Real-Time PCR system (Thermo Fisher Scientific), CFX Connect Real-Time PCR Detection system (Bio-Rad), Eco Real-Time PCR System (Illumina), qTOWER3 G Real-Time System (Analytik Jena), Thermal Cycler Dice Real Time System III (Takara) or 7500 Real-Time PCR System (Thermo Fisher Scientific).

1263

1264 **Animal experiments**

Animal experiments (**Fig. 4 and Extended Data Fig. 3**) were performed as previously described^{2,5,10,23,25,26,30}. Syrian hamsters (male, 4 weeks old) were purchased from Japan SLC Inc. (Shizuoka, Japan). For the virus infection experiments, hamsters were anesthetized by intramuscular injection of a mixture of 0.15 mg/kg medetomidine hydrochloride (Domitor[®], Nippon Zenyaku Kogyo), 2.0 mg/kg midazolam (Dormicum[®], Fujifilm Wako, Cat# 135-13791) and 2.5 mg/kg butorphanol (Vetorphale[®], Meiji Seika Pharma) or 0.15 mg/kg medetomidine hydrochloride, 4.0 mg/kg alphaxalone (Alfaxan[®], Jurox) and 2.5 mg/kg butorphanol. Delta, BA.2.75 and XBB (10,000 TCID₅₀ in 100 µl) or saline (100 µl) was intranasally inoculated under anesthesia. Oral swabs were collected at the indicated timepoints. Body weight was recorded daily by 7 d.p.i. Enhanced pause (Penh), the ratio of time to peak expiratory flow relative to the total expiratory time (Rpef) were measured every day until 7 d.p.i. (see below). Lung tissues were anatomically collected at 2 and 5 d.p.i. The viral RNA load in the oral swabs and respiratory tissues was determined by RT-qPCR. These tissues were also used for IHC and histopathological analyses (see below).

1281

1282 **Lung function test**

Lung function tests (**Fig. 4a**) were routinely performed as previously described^{2,5,10,23,25,26}. The two respiratory parameters (Penh and Rpef) were measured by using a Buxco Small Animal Whole Body Plethysmography system (DSI) according to the manufacturer's instructions. In brief, a hamster was placed in an unrestrained plethysmography chamber and allowed to acclimatize for 30 seconds. Then, data were acquired over a 2.5-minute period by using FinePointe Station and Review software v2.9.2.12849 (DSI).

1290

1291 **Immunohistochemistry**

Immunohistochemistry (IHC) (**Fig. 4c and Extended Data Fig. 3**) was performed as previously described^{2,5,10,23,25,26} using an Autostainer Link 48 (Dako). The deparaffinized sections were exposed to EnVision FLEX target retrieval solution high pH (Agilent, Cat# K8004) for 20 minutes at 97°C for

activation, and a mouse anti-SARS-CoV-2 N monoclonal antibody (clone 1035111, R&D Systems, Cat# MAB10474-SP, 1:400) was used as a primary antibody. The sections were sensitized using EnVision FLEX for 15 minutes and visualized by peroxidase-based enzymatic reaction with 3,3'-diaminobenzidine tetrahydrochloride (Dako, Cat# DM827) as substrate for 5 minutes. The N protein positivity was evaluated by certificated pathologists as previously described^{2,5,10,23,25,26}. Images were incorporated as virtual slides by NDP.scan software v3.2.4 (Hamamatsu Photonics). The N-protein positivity was measured as the area using Fiji software v2.2.0 (ImageJ).

H&E staining

H&E staining (**Fig. 4d**) was performed as previously described^{2,5,10,23,25,26}. Briefly, excised animal tissues were fixed with 10% formalin neutral buffer solution and processed for paraffin embedding. The paraffin blocks were sectioned at a thickness of 3 μ m and then mounted on MAS-GP-coated glass slides (Matsunami Glass, Cat# S9901). H&E staining was performed according to a standard protocol.

Histopathological scoring

Histopathological scoring (**Fig. 4e**) was performed as previously described^{2,5,10,23,25,26}. The inflammation area in the infected lungs was measured by the presence of the type II pneumocyte hyperplasia. Four hamsters infected with each virus were sacrificed on days 2 and 5 d.p.i., and all four lung lobes, including right upper (anterior/cranial), middle, lower (posterior/caudal), and accessory lobes, were sectioned along with their bronchi. The tissue sections were stained by H&E, and the digital microscopic images were incorporated into virtual slides using NDRscan3.2 software (Hamamatsu Photonics). The color of the images was decomposed by RGB in split channels using Fiji software v2.2.0.

Histopathological scoring was performed as described in the previous studies^{2,5,10,23,25,26}. Pathological features including bronchitis or bronchiolitis, hemorrhage or congestion, alveolar damage with epithelial apoptosis and macrophage infiltration, hyperplasia of type II pneumocytes, and the area of the hyperplasia of large type II pneumocytes were evaluated by certified pathologists and the degree of these pathological findings were arbitrarily scored using four-tiered system as 0 (negative), 1 (weak), 2 (moderate), and 3 (severe). The "large type II pneumocytes" are the hyperplasia of type II pneumocytes exhibiting more than 10- μ m-diameter nucleus. Total histology score is the sum of these five indices. In the representative lobe of each lung, the inflammation area with type II pneumocytes was gated by the certificated pathologists on H&E staining, and the indicated area were measured by Fiji software v2.2.0.

1337 **Statistics and reproducibility**

1338 Statistical significance was tested using a two-sided Mann–Whitney *U* test, a
1339 two-sided Student's *t* test, a two-sided Welch's *t* test, or a two-sided paired *t*-test
1340 unless otherwise noted. The tests above were performed using Prism 9 software
1341 v9.1.1 (GraphPad Software).

1342 In the time-course experiments (**Figures 3e–l, 4a–4c, and 4e, and**
1343 **S2b**), a multiple regression analysis including experimental conditions (i.e., the
1344 types of infected viruses) as explanatory variables and timepoints as qualitative
1345 control variables was performed to evaluate the difference between
1346 experimental conditions thorough all timepoints. The initial time point was
1347 removed from the analysis. The *P* value was calculated by a two-sided Wald test.
1348 Subsequently, familywise error rates (FWERs) were calculated by the Holm
1349 method. These analyses were performed in R v4.1.2 (<https://www.r-project.org/>).

1350 Principal component analysis to representing the antigenicity of the S
1351 proteins was performed (**Fig. 2d**). The NT50 values for biological replicates were
1352 scaled, and subsequently, principal component analysis was performed using
1353 the prcomp function on R v4.1.2 (<https://www.r-project.org/>).

1354 In **Figures 5D, 5F and S5**, photographs shown are the representative
1355 areas of at least two independent experiments by using four hamsters at each
1356 timepoint. In **Figure S4D**, photographs shown are the representatives of >20
1357 fields of view taken for each sample.

1358

1359 **Data availability**

1360 All databases/datasets used in this study are available from the GISAID
1361 database (<https://www.gisaid.org>) and GenBank database
1362 (<https://www.gisaid.org>; EPI_SET ID: EPI_SET_221223pb, EPI_SET_221223ew,
1363 EPI_SET_221223yk, EPI_SET_221222mt). Viral genome sequencing data for
1364 working viral stocks are available in the Sequence Read Archive (accession ID:
1365 PRJDB14899).

1366

1367 **Code availability**

1368 The computational codes used in the present study and the GISAID
1369 supplemental tables for EPI_SET_221223pb, EPI_SET_221223ew,
1370 EPI_SET_221223yk, EPI_SET_221222mt are available in the GitHub repository
1371 (<https://github.com/TheSatoLab/XBB>).

1372 References

- 1373 1 WHO. "Tracking SARS-CoV-2 variants (October 28, 2022)"
1374 <https://www.who.int/en/activities/tracking-SARS-CoV-2-variants>. (2022).
- 1375 2 Ito, J. *et al.* Convergent evolution of the SARS-CoV-2 Omicron
1376 subvariants leading to the emergence of BQ.1.1 variant. *BioRxiv*, doi:
1377 <https://doi.org/10.1101/2022.1112.1105.519085> (2022).
- 1378 3 Focosi, D., Quiroga, R., McConnell, S. A., Johnson, M. C. & Casadevall,
1379 A. Convergent evolution in SARS-CoV-2 Spike creates a variant soup
1380 that causes new COVID-19 waves. *BioRxiv*, doi:
1381 <https://doi.org/10.1101/2022.1112.1105.518843> (2022).
- 1382 4 Tuekprakhon, A. *et al.* Antibody escape of SARS-CoV-2 Omicron BA.4
1383 and BA.5 from vaccine and BA.1 serum. *Cell* **185**, 2422-2433 e2413,
1384 doi:10.1016/j.cell.2022.06.005 (2022).
- 1385 5 Kimura, I. *et al.* Virological characteristics of the novel SARS-CoV-2
1386 Omicron variants including BA.4 and BA.5. *Cell* **185**, 3992-4007 e3916
1387 (2022).
- 1388 6 Makowski, E. K., Schardt, J. S., Smith, M. D. & Tessier, P. M. Mutational
1389 analysis of SARS-CoV-2 variants of concern reveals key tradeoffs
1390 between receptor affinity and antibody escape. *PLoS Comput Biol* **18**,
1391 e1010160, doi:10.1371/journal.pcbi.1010160 (2022).
- 1392 7 Aggarwal, A. *et al.* Mechanistic insights into the effects of key mutations
1393 on SARS-CoV-2 RBD-ACE2 binding. *Phys Chem Chem Phys* **23**,
1394 26451-26458, doi:10.1039/d1cp04005g (2021).
- 1395 8 Deshpande, A., Harris, B. D., Martinez-Sobrido, L., Kobie, J. J. & Walter,
1396 M. R. Epitope Classification and RBD Binding Properties of Neutralizing
1397 Antibodies Against SARS-CoV-2 Variants of Concern. *Front Immunol* **12**,
1398 691715, doi:10.3389/fimmu.2021.691715 (2021).
- 1399 9 Chen, J., Wang, R., Wang, M. & Wei, G. W. Mutations Strengthened
1400 SARS-CoV-2 Infectivity. *J Mol Biol* **432**, 5212-5226,
1401 doi:10.1016/j.jmb.2020.07.009 (2020).
- 1402 10 Saito, A. *et al.* Virological characteristics of the SARS-CoV-2 Omicron
1403 BA.2.75 variant. *Cell Host Microbe*, doi:10.1016/j.chom.2022.10.003
1404 (2022).
- 1405 11 Qu, P. *et al.* Evasion of neutralizing antibody responses by the
1406 SARS-CoV-2 BA.2.75 variant. *Cell Host Microbe* **30**, 1518-1526 e1514,
1407 doi:10.1016/j.chom.2022.09.015 (2022).
- 1408 12 Cao, Y. *et al.* Imprinted SARS-CoV-2 humoral immunity induces
1409 convergent Omicron RBD evolution. *BioRxiv*, doi:
1410 <https://doi.org/10.1101/2022.1109.1115.507787> (2022).
- 1411 13 Arora, P. *et al.* Omicron sublineage BQ.1.1 resistance to monoclonal
1412 antibodies. *Lancet Infect Dis*, doi:10.1016/S1473-3099(22)00733-2

- 1413 (2022).
- 1414 14 Wang, Q. *et al.* Antibody evasion by SARS-CoV-2 Omicron subvariants
1415 BA.2.12.1, BA.4, & BA.5. *Nature*, doi:10.1038/s41586-022-05053-w
1416 (2022).
- 1417 15 Cao, Y. *et al.* BA.2.12.1, BA.4 and BA.5 escape antibodies elicited by
1418 Omicron infection. *Nature*, doi:10.1038/s41586-022-04980-y (2022).
- 1419 16 GitHub. "BJ.1/BM.1.1.1 (=BA.2.75.3.1.1.1) recombinant with breakpoint in
1420 S1 [≥ 5 sequences, 3x Singapore, 2x US as of 2022-09-12] (September
1421 13, 2022)".
1422 <https://github.com/cov-lineages/pango-designation/issues/1058>. (2022).
- 1423 17 WHO. "TAG-VE statement on Omicron sublineages BQ.1 and XBB
1424 (October 27, 2022)"
1425 [https://www.who.int/news/item/27-10-2022-tag-ve-statement-on-omicron-](https://www.who.int/news/item/27-10-2022-tag-ve-statement-on-omicron-sublineages-bq.1-and-xbb)
1426 [sublineages-bq.1-and-xbb](https://www.who.int/news/item/27-10-2022-tag-ve-statement-on-omicron-sublineages-bq.1-and-xbb). (2022).
- 1427 18 Wang, Q. *et al.* Antigenic characterization of the SARS-CoV-2 Omicron
1428 subvariant BA.2.75. *Cell Host Microbe* **30**, 1512-1517 e1514,
1429 doi:10.1016/j.chom.2022.09.002 (2022).
- 1430 19 Martin, D. P. *et al.* RDP5: a computer program for analyzing
1431 recombination in, and removing signals of recombination from, nucleotide
1432 sequence datasets. *Virus Evol* **7**, veaa087, doi:10.1093/ve/veaa087
1433 (2021).
- 1434 20 GitHub. "BE.1.1.1 sublineage with Orf1b:Y264H and S:N460K (69
1435 sequences) emerged in Nigeria (14 seqs) (August 26, 2022)".
1436 <https://github.com/cov-lineages/pango-designation/issues/993>. (2022).
- 1437 21 Dejnirattisai, W. *et al.* SARS-CoV-2 Omicron-B.1.1.529 leads to
1438 widespread escape from neutralizing antibody responses. *Cell* **185**,
1439 467-484 e415, doi:10.1016/j.cell.2021.12.046 (2022).
- 1440 22 Zahradnik, J. *et al.* SARS-CoV-2 variant prediction and antiviral drug
1441 design are enabled by RBD in vitro evolution. *Nat Microbiol* **6**, 1188-1198,
1442 doi:10.1038/s41564-021-00954-4 (2021).
- 1443 23 Yamasoba, D. *et al.* Virological characteristics of the SARS-CoV-2
1444 Omicron BA.2 spike. *Cell*, doi:10.1016/j.cell.2022.04.035 (2022).
- 1445 24 Motozono, C. *et al.* SARS-CoV-2 spike L452R variant evades cellular
1446 immunity and increases infectivity. *Cell Host Microbe* **29**, 1124-1136,
1447 doi:10.1016/j.chom.2021.06.006 (2021).
- 1448 25 Suzuki, R. *et al.* Attenuated fusogenicity and pathogenicity of
1449 SARS-CoV-2 Omicron variant. *Nature*, doi:10.1038/s41586-022-04462-1
1450 (2022).
- 1451 26 Saito, A. *et al.* Enhanced fusogenicity and pathogenicity of SARS-CoV-2
1452 Delta P681R mutation. *Nature* **602**, 300-306,
1453 doi:10.1038/s41586-021-04266-9 (2022).

- 1454 27 Nasser, H. *et al.* Monitoring fusion kinetics of viral and target cell
1455 membranes in living cells using a SARS-CoV-2 spike-protein-mediated
1456 membrane fusion assay. *STAR Protoc* **3**, 101773,
1457 doi:10.1016/j.xpro.2022.101773 (2022).
- 1458 28 Kimura, I. *et al.* The SARS-CoV-2 spike S375F mutation characterizes
1459 the Omicron BA.1 variant. *iScience* **25**, 105720,
1460 doi:10.1016/j.isci.2022.105720 (2022).
- 1461 29 Hashimoto, R. *et al.* SARS-CoV-2 disrupts the respiratory vascular barrier
1462 by suppressing Claudin-5 expression. *Sci Adv* **8**, eabo6783, doi:doi:
1463 10.1126/sciadv.abo6783 (2022).
- 1464 30 Tamura, T. *et al.* Comparative pathogenicity of SARS-CoV-2 Omicron
1465 subvariants including BA.1, BA.2, and BA.5. *BioRxiv*, doi:
1466 <https://doi.org/10.1101/2022.1108.1105.502758> (2022).
- 1467 31 Uriu, K. *et al.* Neutralization of the SARS-CoV-2 Mu variant by
1468 convalescent and vaccine serum. *N Engl J Med* **385**, 2397-2399,
1469 doi:10.1056/NEJMc2114706 (2021).
- 1470 32 Uriu, K. *et al.* Characterization of the immune resistance of SARS-CoV-2
1471 Mu variant and the robust immunity induced by Mu infection. *J Infect Dis*,
1472 doi:10.1093/infdis/jiac053 (2022).
- 1473 33 Cerutti, G. *et al.* Potent SARS-CoV-2 neutralizing antibodies directed
1474 against spike N-terminal domain target a single supersite. *Cell Host*
1475 *Microbe* **29**, 819-833 e817, doi:10.1016/j.chom.2021.03.005 (2021).
- 1476 34 Sasaki, A., Lion, S. & Boots, M. Antigenic escape selects for the evolution
1477 of higher pathogen transmission and virulence. *Nat Ecol Evol* **6**, 51-62,
1478 doi:10.1038/s41559-021-01603-z (2022).
- 1479 35 Ozono, S. *et al.* SARS-CoV-2 D614G spike mutation increases entry
1480 efficiency with enhanced ACE2-binding affinity. *Nat Commun* **12**, 848,
1481 doi:10.1038/s41467-021-21118-2 (2021).
- 1482 36 Ferreira, I. *et al.* SARS-CoV-2 B.1.617 mutations L452R and E484Q are
1483 not synergistic for antibody evasion. *J Infect Dis* **224**, 989-994,
1484 doi:10.1093/infdis/jiab368 (2021).
- 1485 37 Matsuyama, S. *et al.* Enhanced isolation of SARS-CoV-2 by
1486 TMPRSS2-expressing cells. *Proc Natl Acad Sci U S A* **117**, 7001-7003,
1487 doi:10.1073/pnas.2002589117 (2020).
- 1488 38 Fujita, S. *et al.* Structural Insight into the Resistance of the SARS-CoV-2
1489 Omicron BA.4 and BA.5 Variants to Cilgavimab. *Viruses* **14**, 2677 (2022).
- 1490 39 Chen, S., Zhou, Y., Chen, Y. & Gu, J. fastp: an ultra-fast all-in-one
1491 FASTQ preprocessor. *Bioinformatics* **34**, i884-i890,
1492 doi:10.1093/bioinformatics/bty560 (2018).
- 1493 40 Li, H. & Durbin, R. Fast and accurate short read alignment with
1494 Burrows-Wheeler transform. *Bioinformatics* **25**, 1754-1760,

doi:10.1093/bioinformatics/btp324 (2009).

41 Li, H. *et al.* The sequence alignment/map format and SAMtools. *Bioinformatics* **25**, 2078-2079, doi:10.1093/bioinformatics/btp352 (2009).

42 Cingolani, P. *et al.* A program for annotating and predicting the effects of single nucleotide polymorphisms, SnpEff: SNPs in the genome of *Drosophila melanogaster* strain w1118; iso-2; iso-3. *Fly (Austin)* **6**, 80-92, doi:10.4161/fly.19695 (2012).

43 Lanfear, R. A global phylogeny of SARS-CoV-2 sequences from GISAID. Zenodo doi: 10.5281/zenodo.3958883. <https://zenodo.org/record/4289383#.Y6ER8C33ITs>. (2020).

44 Katoh, K. & Standley, D. M. MAFFT multiple sequence alignment software version 7: improvements in performance and usability. *Mol Biol Evol* **30**, 772-780, doi:10.1093/molbev/mst010 (2013).

45 Martin, D. & Rybicki, E. RDP: detection of recombination amongst aligned sequences. *Bioinformatics* **16**, 562-563, doi:10.1093/bioinformatics/16.6.562 (2000).

46 Padidam, M., Sawyer, S. & Fauquet, C. M. Possible emergence of new geminiviruses by frequent recombination. *Virology* **265**, 218-225, doi:10.1006/viro.1999.0056 (1999).

47 Posada, D. & Crandall, K. A. Evaluation of methods for detecting recombination from DNA sequences: computer simulations. *Proc Natl Acad Sci U S A* **98**, 13757-13762, doi:10.1073/pnas.241370698 (2001).

48 Smith, J. M. Analyzing the mosaic structure of genes. *J Mol Evol* **34**, 126-129, doi:10.1007/BF00182389 (1992).

49 Boni, M. F., Posada, D. & Feldman, M. W. An exact nonparametric method for inferring mosaic structure in sequence triplets. *Genetics* **176**, 1035-1047, doi:10.1534/genetics.106.068874 (2007).

50 Martin, D. P., Posada, D., Crandall, K. A. & Williamson, C. A modified bootscan algorithm for automated identification of recombinant sequences and recombination breakpoints. *AIDS Res Hum Retroviruses* **21**, 98-102, doi:10.1089/aid.2005.21.98 (2005).

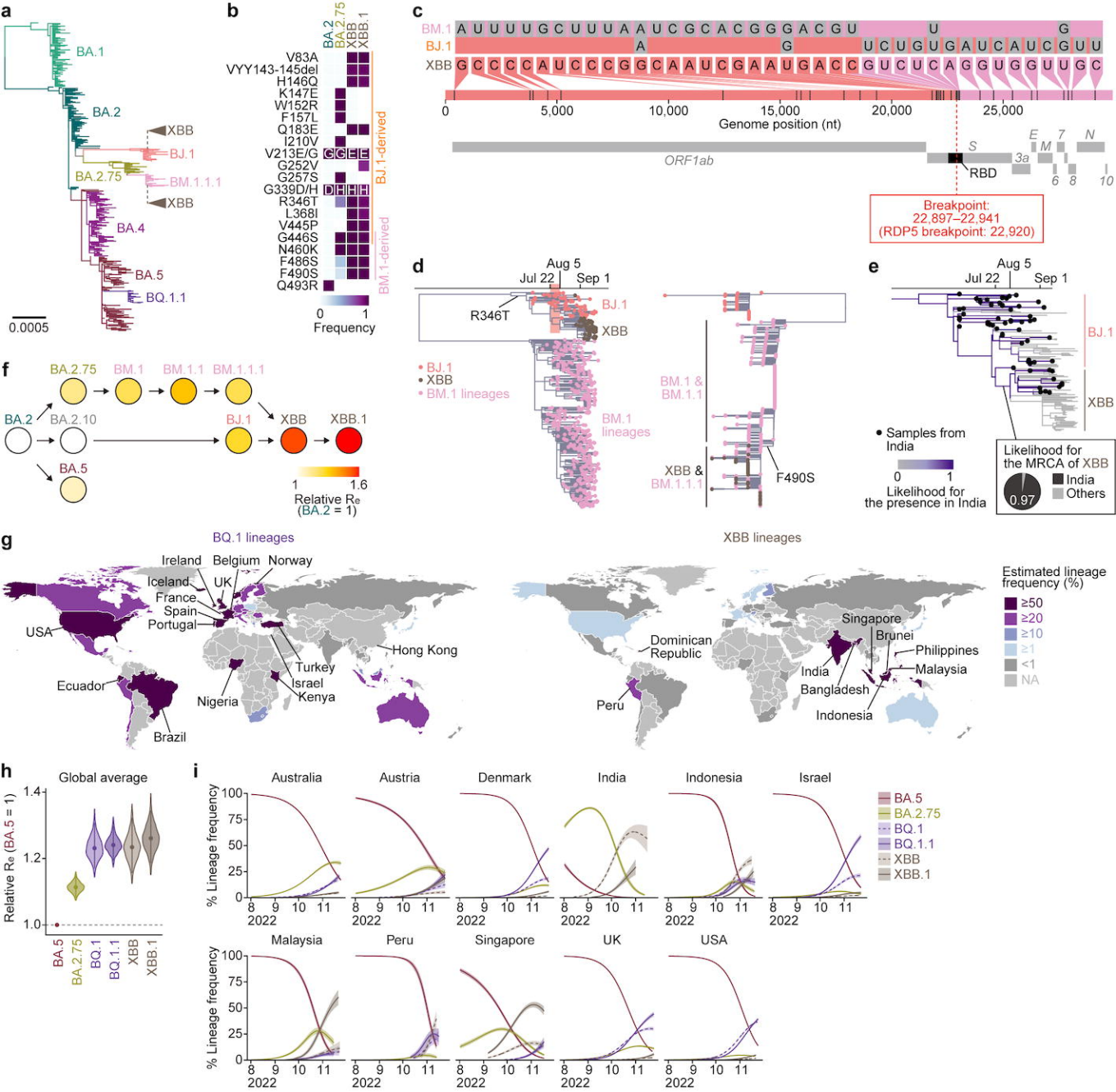
51 Gibbs, M. J., Armstrong, J. S. & Gibbs, A. J. Sister-scanning: a Monte Carlo procedure for assessing signals in recombinant sequences. *Bioinformatics* **16**, 573-582, doi:10.1093/bioinformatics/16.7.573 (2000).

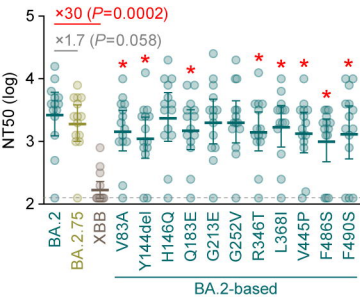
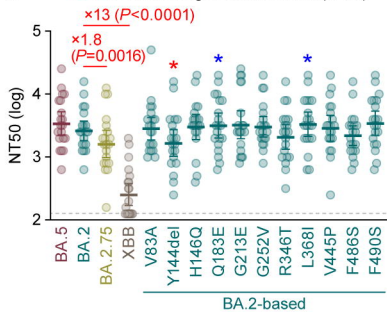
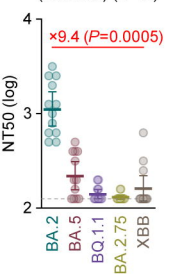
52 Price, M. N., Dehal, P. S. & Arkin, A. P. FastTree 2--approximately maximum-likelihood trees for large alignments. *PLoS One* **5**, e9490, doi:10.1371/journal.pone.0009490 (2010).

53 Nguyen, L. T., Schmidt, H. A., von Haeseler, A. & Minh, B. Q. IQ-TREE: a fast and effective stochastic algorithm for estimating maximum-likelihood phylogenies. *Mol Biol Evol* **32**, 268-274, doi:10.1093/molbev/msu300 (2015).

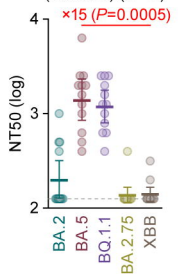
- 1536 54 Rambaut, A., Lam, T. T., Max Carvalho, L. & Pybus, O. G. Exploring the
1537 temporal structure of heterochronous sequences using TempEst
1538 (formerly Path-O-Gen). *Virus Evol* **2**, vew007, doi:10.1093/ve/vew007
1539 (2016).
- 1540 55 Sagulenko, P., Puller, V. & Neher, R. A. TreeTime: Maximum-likelihood
1541 phylodynamic analysis. *Virus Evol* **4**, vex042, doi:10.1093/ve/vex042
1542 (2018).
- 1543 56 Duchene, S. *et al.* Temporal signal and the phylodynamic threshold of
1544 SARS-CoV-2. *Virus Evol* **6**, veaa061, doi:10.1093/ve/veaa061 (2020).
- 1545 57 Louca, S. & Doebeli, M. Efficient comparative phylogenetics on large
1546 trees. *Bioinformatics* **34**, 1053-1055, doi:10.1093/bioinformatics/btx701
1547 (2018).
- 1548 58 Kimura, I. *et al.* The SARS-CoV-2 Lambda variant exhibits enhanced
1549 infectivity and immune resistance. *Cell Rep* **38**, 110218,
1550 doi:10.1016/j.celrep.2021.110218 (2022).
- 1551 59 Niwa, H., Yamamura, K. & Miyazaki, J. Efficient selection for
1552 high-expression transfectants with a novel eukaryotic vector. *Gene* **108**,
1553 193-199, doi:10.1016/0378-1119(91)90434-d (1991).
- 1554 60 Yamasoba, D. *et al.* Neutralisation sensitivity of SARS-CoV-2 omicron
1555 subvariants to therapeutic monoclonal antibodies. *Lancet Infect Dis* **22**,
1556 942-943, doi:10.1016/S1473-3099(22)00365-6 (2022).
- 1557 61 Meng, B. *et al.* Altered TMPRSS2 usage by SARS-CoV-2 Omicron
1558 impacts tropism and fusogenicity. *Nature*,
1559 doi:10.1038/s41586-022-04474-x (2022).
- 1560 62 Reed, L. J. & Muench, H. A simple method of estimating fifty percent
1561 endpoints. *Am J Hygiene* **27**, 493-497 (1938).
- 1562 63 Zahradnik, J. *et al.* A protein-engineered, enhanced yeast display
1563 platform for rapid evolution of challenging targets. *ACS Synth Biol* **10**,
1564 3445-3460, doi:10.1021/acssynbio.1c00395 (2021).
- 1565 64 Ozono, S., Zhang, Y., Tobiume, M., Kishigami, S. & Tokunaga, K.
1566 Super-rapid quantitation of the production of HIV-1 harboring a
1567 luminescent peptide tag. *J Biol Chem* **295**, 13023-13030,
1568 doi:10.1074/jbc.RA120.013887 (2020).
- 1569 65 Kondo, N., Miyauchi, K. & Matsuda, Z. Monitoring viral-mediated
1570 membrane fusion using fluorescent reporter methods. *Curr Protoc Cell*
1571 *Biol* **Chapter 26**, Unit 26 29, doi:10.1002/0471143030.cb2609s50 (2011).
- 1572 66 Sano, E. *et al.* Cell response analysis in SARS-CoV-2 infected bronchial
1573 organoids. *Commun Biol* **5**, 516, doi:10.1038/s42003-022-03499-2
1574 (2022).
- 1575 67 Yamamoto, Y. *et al.* Long-term expansion of alveolar stem cells derived
1576 from human iPS cells in organoids. *Nat Methods* **14**, 1097-1106,

1577 doi:10.1038/nmeth.4448 (2017).
1578 68 Konishi, S. *et al.* Directed induction of functional multi-ciliated cells in
1579 proximal airway epithelial spheroids from human pluripotent stem cells.
1580 *Stem Cell Reports* **6**, 18-25, doi:10.1016/j.stemcr.2015.11.010 (2016).
1581 69 Gotoh, S. *et al.* Generation of alveolar epithelial spheroids via isolated
1582 progenitor cells from human pluripotent stem cells. *Stem Cell Reports* **3**,
1583 394-403, doi:10.1016/j.stemcr.2014.07.005 (2014).
1584 70 Deguchi, S. *et al.* Usability of polydimethylsiloxane-based microfluidic
1585 devices in pharmaceutical research using human hepatocytes. *ACS*
1586 *Biomater Sci Eng* **7**, 3648-3657, doi:10.1021/acsbiomaterials.1c00642
1587 (2021).
1588

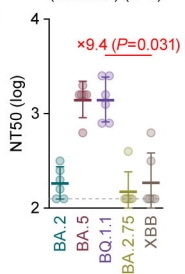


a BA.2 breakthrough infection sera (n=14)**b** BA.5 breakthrough infection sera (n=20)**c** BA.2 infection sera (hamster) (n=12)

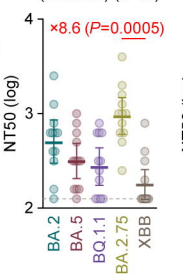
BA.5 infection sera (hamster) (n=12)



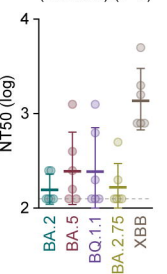
BQ.1.1 infection sera (hamster) (n=6)



BA.2.75 infection sera (hamster) (n=12)



XBB infection sera (hamster) (n=6)

**d** Antigenic cartography